Nonaxisymmetric magnetorotational instability in spherical Couette flow

Domenico G. Meduri,* François Lignières, and Laurène Jouve
Institut de Recherche en Astrophysique et Planétologie, Université de Toulouse, CNRS, UPS, CNES, 31400 Toulouse, France

(Received 4 November 2018; published 22 July 2019)

We investigate numerically the flow of an electrically conducting fluid in a rapidly rotating spherical shell where the inner boundary spins slightly faster than the outer one. The magnetic field evolves self-consistently from an initial dipolar configuration of weak amplitude, and a toroidal field is produced by winding this poloidal field through the internal differential rotation. First, we characterize the axisymmetric field solutions obtained at long times when the Lorentz force is negligible and the flow follows the steady, purely hydrodynamical solution. We then examine the stability of these solutions, focusing on the regime of large magnetic Reynolds numbers where the field is dominantly toroidal. When the ratio of the azimuthal Alfvén frequency to the rotation frequency exceeds a certain value, a nonaxisymmetric instability develops. We show that the instability properties are compatible with those expected for the magnetorotational instability. Finally, we compare the instability properties with predictions obtained from a local linear stability analysis. The linear analysis agrees well with the numerical simulation results, except in a number of cases where the discrepancies are attributed to shearing effects on the unstable modes.

DOI: 10.1103/PhysRevE.100.013110

I. INTRODUCTION

Spherical Couette flow is the flow of a viscous fluid contained in a spherical shell whose boundaries rotate rigidly about a common axis with different angular velocities. Since the second half of the past century, this flow has been extensively studied analytically, experimentally, and, only more recently, numerically. Despite the seeming simplicity of the problem, a wide variety of flow solutions and instabilities exists depending on the shell aspect ratio and boundary rotation speeds. If the fluid is electrically conducting and a magnetic field is present, magnetohydrodynamic (MHD) effects can lead to different solutions and distinct types of instabilities. In this work we examine several aspects of this MHD problem, from axisymmetric flow and field solutions to their stability.

From an astrophysical perspective, magnetic spherical Couette flow is attractive to study how magnetic fields interact with differentially rotating flows in a geometry relevant for stellar and planetary interiors. Magnetic fields and differential rotation are indeed known to exist in the internal regions of planets and stars, with prime examples being the Earth's core, the liquid interior of giant planets, and the solar convection zone. A weak differential rotation between the Earth's inner core and the mantle, presumably of less than 1° per year, has been revealed by seismic studies [1,2]. The alternating bands of zonal winds observed on the surface of Jupiter and Saturn are also likely manifestations of differential rotation patterns in the liquid interior of these planets. Within the convective envelope of the Sun, differential rotation is relatively strong, largely varies with radius and latitude, and is generally ascribed to the redistribution of angular momentum produced by convective motions.

In stars other than the Sun, a certain degree of differential rotation is expected as a consequence of their evolution. The contracting core and inflating envelope of subgiant and red giant stars, for example, would generate large internal rotation contrasts if angular momentum was to be conserved. Recent asteroseismic studies of these stellar populations using data from the Kepler satellite, however, revealed absolute internal rotations and core to envelope rotation contrasts much weaker than expected [3–5]. An efficient angular momentum redistribution and/or extraction must then have occurred during earlier stages of the stellar evolution. Purely hydrodynamical models considering the transport of angular momentum induced by meridional flows and shear instabilities have been proven inefficient at imposing such small internal rotations (see, e.g., [6]). Magnetic processes, such as the enhanced turbulence generated by MHD instabilities, could instead provide a viable alternative for increasing the internal angular momentum redistribution [7–9].

In the classical hydrodynamical Couette flow configuration analyzed by Proudman [10] and Stewartson [11], the outer boundary rotates arbitrarily fast and the inner boundary spins slightly faster in the same direction. In this asymptotic regime, the interior flow solution is driven by the viscous Ekman boundary layers and develops a free shear layer, known as the Stewartson layer, attached to the tangent cylinder (the cylindrical surface parallel to the rotation axis and tangent to the inner boundary at the equator). Hollerbach [12] investigated numerically the effect of an imposed dipolar magnetic field on this hydrodynamical solution and found that the Stewartson layer is completely suppressed when magnetic forces are of leading order. A variety of other magnetically induced flow configurations exists depending on the imposed magnetic field geometry and electromagnetic boundary conditions [13–15]. These include superrotating and counterrotating jets, confined regions of the interior flow which rotate faster than the two

*domenico.meduri@irap.omp.eu

boundaries in the prograde and retrograde directions, respectively. Nonaxisymmetric instabilities of these basic state configurations have been analyzed in the past (e.g., [16,17]) and some of them are reminiscent of those observed in laboratory experiments with liquid sodium [18–20].

Magnetic spherical Couette flow is in principle susceptible to magnetorotational instability (MRI). In its original formulation by Velikhov [21] and Chandrasekhar [22], the MRI is an axisymmetric instability due to a weak axial magnetic field threading a hydrodynamically stable Taylor-Couette flow, the flow of a viscous fluid sheared between two coaxial rotating cylinders, where the mean angular velocity decreases outwards. Balbus and Hawley [23] first recognized the importance of the MRI in the context of accretion disks, suggesting that it is the main source of turbulence and outward angular momentum transport. Since then, this instability has been extensively studied.

In the presence of azimuthal magnetic fields, nonaxisymmetric versions of the MRI can be triggered [24–29]. Robust evidence of the expected nonaxisymmetric MRI modes in purely azimuthal fields was obtained in the liquid metal Taylor-Couette experiment of Seilmayer *et al.* [30]. In spherical Couette experiments, Sisan *et al.* [31] claim to have obtained nonaxisymmetric MRI, but the observed global modes are probably related to boundary-driven instabilities instead [32,33].

Most MRI studies focus on regimes relevant for accretion disks and are thus not directly applicable to stellar and planetary interiors. In the Earth's outer core, for example, differential rotation is much weaker than in accretion disks and resistive effects are considerably larger. Most importantly, planetary cores are far from being weakly magnetized since they are expected to be in magnetostrophic balance, a state where the Coriolis and Lorentz forces partially cancel. In this regime, Petitdemange *et al.* [34,35] showed that a modified version of the MRI can nevertheless be excited, in the presence of a purely axial field but also for combined axial and azimuthal fields.

Whereas several studies investigate the basic states and instabilities of magnetic spherical Couette flow relevant to laboratory experiments, i.e., with imposed axial or dipolar magnetic fields, the same cannot be said for more complex field geometries and for configurations where the field evolves self-consistently in time, as expected in astrophysical situations. Moreover, recent numerical works focus on exploring the hydrodynamically unstable regime, characterized by large boundary differential rotations, where dynamo action has been found to be possible in both wide [36] and thin [37] shell gaps. In this regime, helical flows produced by hydrodynamical instabilities are responsible for dynamo action. However, MHD instabilities of hydrodynamically stable shear flows such as MRI are also capable of generating self-sustained magnetic fields (see, e.g., [38,39]).

In this study we perform three-dimensional numerical simulations of a spherical Couette flow which is hydrodynamically stable and mostly compatible with the Proudman and Stewartson asymptotic regime mentioned above. We then investigate numerically the ability of different magnetic field configurations, which evolve self-consistently, to destabilize such flow. A weak axial dipole field, used as the initial condition, is wound within the Stewartson layer, producing an axisymmetric azimuthal field. The initial dipole field strength is kept weak enough that the Lorentz force has a mild or negligible impact on the flow which remains close to the purely hydrodynamical Proudman-Stewartson solution. We first characterize the axisymmetric, mixed poloidal and toroidal field configurations obtained when varying the boundary rotation rates and rotation contrast, as well as the fluid kinematic viscosity and magnetic diffusivity. Then we examine the stability of the dominantly toroidal field configurations. A comparison of the numerical results with theoretical predictions obtained from a local linear stability analysis of the MHD equations is also discussed.

The remainder of this paper is organized as follows. In Sec. II we describe the model formulation and the numerical technique used to solve the equations. In Sec. III the purely hydrodynamical solutions obtained in the explored parameter range are compared with the Proudman and Stewartson asymptotic solution. In Sec. IV we discuss the axisymmetric field solutions obtained when varying the input model parameters and we investigate the force balances leading to such solutions. The stability of the dominantly toroidal field configurations is analyzed in Sec. V. We interpret the nonaxisymmetric instability found in the numerical simulations in Sec. VI, where we provide evidence for MRI. The instability properties are further characterized using the local linear stability analysis of Acheson [40]. The paper closes with a summary of the results and a discussion of their relevance in the astrophysical context and to laboratory experiments (Sec. VII).

II. MODEL FORMULATION

In this study we consider magnetic spherical Couette flow. An incompressible, viscous, and resistive fluid fills a wide-gap spherical shell where the inner and outer boundaries rotate rigidly about the vertical axis with angular velocities Ω_i and Ω_o, respectively. The inner boundary rotates faster than the outer one and in the same direction, with the rotation contrast defined as $\Delta\Omega = \Omega_i - \Omega_o > 0$. The initial condition for the magnetic field is an axial dipole field. In the frame of reference corotating with the outer boundary, the dimensionless equations governing the system are the momentum equation

$$\mathrm{Ro}\left(\frac{\partial \mathbf{u}}{\partial t} + \mathbf{u}\cdot\boldsymbol{\nabla}\mathbf{u}\right) = -\boldsymbol{\nabla} p - 2\hat{\mathbf{e}}_z \times \mathbf{u} + \mathrm{Ek}\,\nabla^2\mathbf{u} + \frac{\mathrm{Lo}_0^2}{\mathrm{Ro}}(\boldsymbol{\nabla}\times\mathbf{B})\times\mathbf{B}, \tag{1}$$

the continuity equation

$$\boldsymbol{\nabla}\cdot\mathbf{u} = 0, \tag{2}$$

the magnetic induction equation

$$\frac{\partial \mathbf{B}}{\partial t} = \boldsymbol{\nabla}\times(\mathbf{u}\times\mathbf{B}) + \frac{\mathrm{Ek}}{\mathrm{Ro}\,\mathrm{Pm}}\nabla^2\mathbf{B}, \tag{3}$$

and the solenoidal condition for the magnetic field

$$\boldsymbol{\nabla}\cdot\mathbf{B} = 0. \tag{4}$$

Here $\mathbf{u}$ is the dimensionless velocity, p a modified dimensionless pressure which includes the centrifugal force, $\hat{\mathbf{e}}_z$ the unit vector in the direction of the rotation axis, and $\mathbf{B}$ the dimensionless magnetic field. The shell thickness $d = r_o - r_i$, where r_i and r_o are the inner and outer boundary radii, respectively, is used as the reference length scale and $\Delta\Omega^{-1}$ as the timescale. The magnetic field is scaled with B_0, the absolute initial dipole field strength at the poles of the inner boundary.

Five dimensionless numbers control the problem. The first is the system aspect ratio $a = r_i/r_o$, which is fixed to 0.3 in this study. The Ekman number

$$\mathrm{Ek} = \frac{\nu}{\Omega_o d^2} \tag{5}$$

quantifies the relative importance of viscous to Coriolis forces in the momentum equation. It can also be interpreted as the ratio of the global rotation timescale $t_\Omega = 1/\Omega_o$ to the viscous diffusion time $t_\nu = d^2/\nu$, where ν is the fluid kinematic viscosity. The Rossby number

$$\mathrm{Ro} = \frac{\Delta\Omega}{\Omega_o} \tag{6}$$

defines the rotation contrast between the two boundaries relative to the outer boundary rotation rate. The magnetic Prandtl number

$$\mathrm{Pm} = \frac{\nu}{\eta} \tag{7}$$

specifies the kinematic viscosity relative to the fluid magnetic diffusivity η. The last control parameter is

$$\mathrm{Lo}_0 = \frac{B_0}{\sqrt{\mu\rho}d\Omega_o} \tag{8}$$

and can be interpreted as the ratio of the rotation timescale t_Ω to the Alfvén crossing time based on the initial dipole field $t_\mathrm{A} = \sqrt{\mu\rho}d/B_0$. Here μ denotes the magnetic permeability of vacuum and ρ the (constant) fluid density. This dimensionless number is sometimes referred to as the Lorentz number (e.g., [41]) and we adhere to this nomenclature here.

In the following, the magnetic Reynolds number

$$\mathrm{Rm} = \frac{\Delta\Omega d^2}{\eta} \tag{9}$$

will also be of particular interest. It is related to the above control parameters by $\mathrm{Rm} = \mathrm{Ro}\,\mathrm{Pm}/\mathrm{Ek}$.

We assume no-slip flow boundary conditions typical of spherical Couette studies, that is, $\mathbf{u} = \mathbf{0}$ at radius $r = r_o/d$ and $\mathbf{u} = (r_i/d)\sin\theta\,\hat{\mathbf{e}}_\varphi$ at $r = r_i/d$. Here (r, θ, φ) denote dimensionless spherical coordinates and $\hat{\mathbf{e}}_\varphi$ is the unit vector in the azimuthal direction. The exterior of the fluid domain is assumed to be electrically insulating. The magnetic field boundary conditions are therefore appropriate to match a potential field outside the fluid volume.

The above system of equations and boundary conditions is solved numerically using the pseudospectral MHD code MagIC [42,43] (publicly available from [44]). Since a detailed description of the employed numerical techniques is given by Christensen and Wicht [45], we outline only the essentials here. MagIC employs a spherical harmonic decomposition in the azimuthal and latitudinal directions. Chebyshev polynomials are used in the radial direction to guarantee a denser grid towards r_i and r_o where boundary layers need to be resolved. The equations are integrated in time using a mixed implicit-explicit time stepping scheme. A numerical resolution of $N_r = 257$ radial grid points with a maximum spherical harmonic degree $\ell_\mathrm{max} = 170$ typically suffices to resolve the less diffusive and thus most computationally demanding nonaxisymmetric runs considered in the following.

III. AXISYMMETRIC NONMAGNETIC SOLUTIONS

In this section we present the hydrodynamical flow solutions ($\mathrm{Lo}_0 = 0$) obtained when varying the Ekman and Rossby numbers. The flow regime we consider is characterized by fast rotations ($\mathrm{Ek} \ll 1$) and small to moderate differential rotations ($\mathrm{Ro} \leqslant 0.2$). In this regime the flow is hydrodynamically stable to nonaxisymmetric perturbations, as discussed at the end of this section. The Ekman numbers explored are $\mathrm{Ek} = 10^{-4}$ and 10^{-5}. Smaller values are too computationally demanding for a systematic parameter study.

For slight differential rotations ($\mathrm{Ro} \ll 1$), Proudman [10] and Stewartson [11] described stationary and axisymmetric analytical solutions valid in this limit where the Coriolis force dominates over inertial and viscous forces in most parts of the interior. Such flow satisfies the Proudman-Taylor constraint of vertically invariant motions

$$\mathbf{u} = u_\varphi(s)\hat{\mathbf{e}}_\varphi + s^{-1}\nabla\psi(s) \times \hat{\mathbf{e}}_\varphi. \tag{10}$$

In the above equation $s = r\sin\theta$ defines the dimensionless cylindrical radial coordinate and ψ is the stream function which defines the poloidal flow velocity $\mathbf{u}_p = s^{-1}\nabla\psi(s) \times \hat{\mathbf{e}}_\varphi$. The numerical flow solution at $\mathrm{Ro} = 2.5 \times 10^{-4}$ is illustrated in Fig. 1 for the two Ekman numbers explored. Left and right panels show the rotation rate $\Omega' = u_\varphi/s$ and the meridional flow, respectively. In the interior, the flow is largely vertically invariant as expected. The tangent cylinder (TC) is the cylindrical surface parallel to the rotation axis and tangent to the inner boundary at the equator. Outside the TC, the asymptotic state is rigid rotation with the same angular velocity as the outer boundary. Inside the TC, the fluid mainly rotates at $\Omega' = 1/2$. Ekman layers of thickness $\mathrm{Ek}^{1/2}$ adjust the azimuthal flow inside the TC to the spherical boundary rotation rates. Centrifugal forces drive the fluid towards the equator inside the inner Ekman layer and towards the rotation axis inside the outer Ekman layer. This secondary flow produces a large-scale counterclockwise (clockwise) meridional circulation in the northern (southern) hemisphere. This meridional flow is weak compared to the $O(1)$ azimuthal flow, being of $O(\mathrm{Ek}^{1/2})$ in amplitude. Close to the rotation axis, the meridional circulation goes from the outer Ekman layer vertically down to the inner Ekman layer. Close to the TC, a narrow jet allows the flow to recirculate from the inner Ekman layer to the outer one.

We now compare the numerical solutions in the interior with the analytical solution obtained by Proudman [10]. Outside the TC ($s \geqslant r_i/d$) where the flow is in rigid rotation,

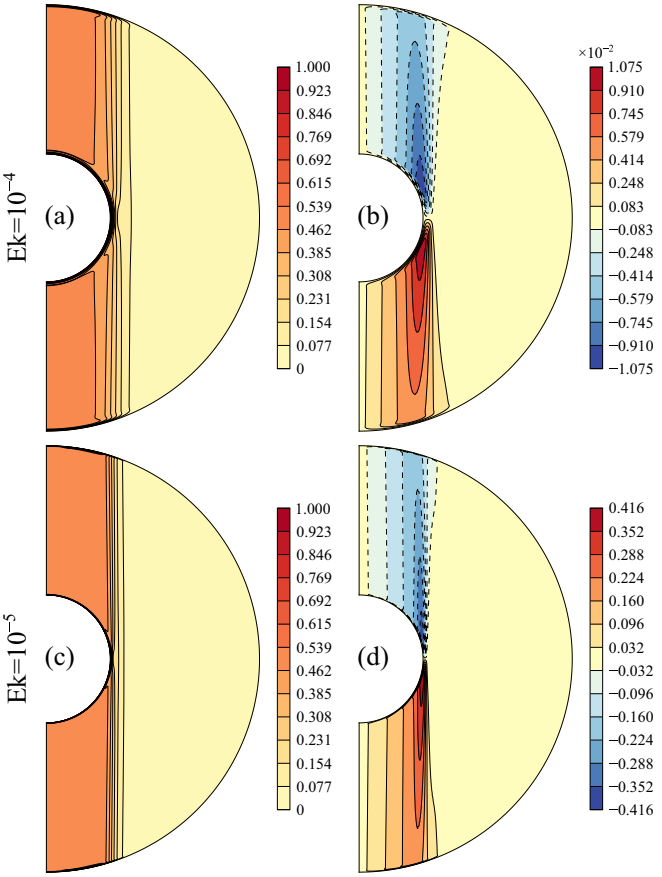

FIG. 1. Nonmagnetic ($\mathrm{Lo}_0 = 0$) axisymmetric flow solutions at a Rossby number $\mathrm{Ro} = 2.5 \times 10^{-4}$. (a) and (b) for an Ekman number $\mathrm{Ek} = 10^{-4}$, (c) and (d) for $\mathrm{Ek} = 10^{-5}$. (a) and (c) display the angular velocity Ω', and (b) and (d) the meridional circulation (counterclockwise in the northern hemisphere and clockwise in the southern hemisphere). These solutions are representative of the asymptotic regime of Proudman [10] and Stewartson [11], characterized by fast outer boundary rotations and slightly faster inner boundary rotations.

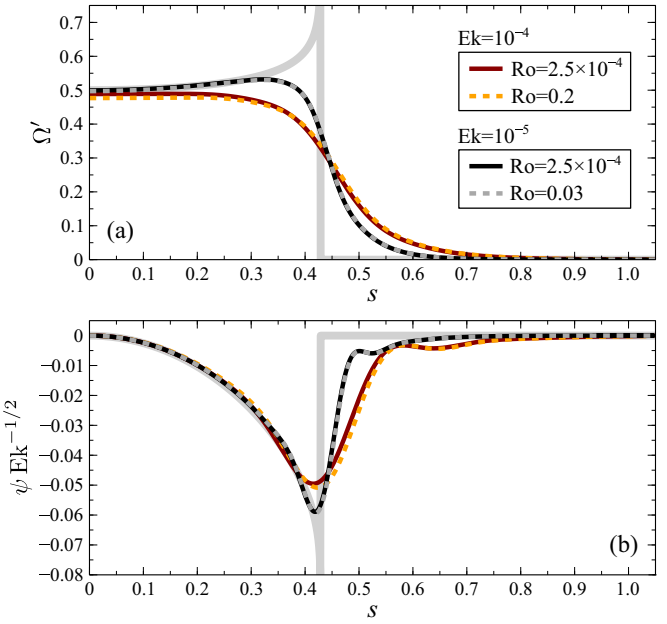

FIG. 2. Comparison of the asymptotic solution of Proudman [10] with different nonmagnetic numerical flow solutions. (a) and (b) show, respectively, the angular velocity Ω' and the stream function ψ as function of the cylindrical radial coordinate s. Solid gray curves display Proudman's solution as given in Eqs. (11a)–(11d). This solution is discontinuous at the tangent cylinder location. For each Ekman number case, solid and dashed curves illustrate numerical solutions at a small Rossby number $\mathrm{Ro} = 2.5 \times 10^{-4}$ and at the largest Ro explored in this study, respectively [see the legend in (a)]. The numerical solutions are taken at a depth of $z = r_o/2d$, where z is the dimensionless cylindrical vertical coordinate.

we have

$$\Omega'(s) = 0, \tag{11a}$$

$$\psi(s) = 0. \tag{11b}$$

For $s < r_i/d$, the angular velocity and the stream function are, respectively,

$$\Omega'(s) = \frac{(1-s^2)^{1/4}}{(1-s^2)^{1/4} + [1-(a^{-1}-1)^2 s^2]^{1/4}} \tag{11c}$$

and

$$\psi(s) = \frac{\mathrm{Ek}^{1/2}}{2} \frac{s^2}{(1-s^2)^{1/4} + [1-(a^{-1}-1)^2 s^2]^{1/4}}. \tag{11d}$$

This analytical solution is shown in Fig. 2 by the thick gray curves, whereas numerical solutions at the small Rossby number discussed above are displayed as solid curves. At the two Ekman numbers explored, the angular velocity jump at the TC is still significantly smaller than its asymptotic value. A closer match with the asymptotic solution is obtained for the smaller Ekman number of $\mathrm{Ek} = 10^{-5}$ as expected.

The discontinuity in the interior flow across the TC is resolved within a free shear layer, known as the Stewartson layer [11]. The Stewartson layer is composed of three nested sublayers. The outermost sublayer of thickness $\mathrm{Ek}^{1/4}$ is located just outside the TC and accommodates the main jump in the azimuthal velocity. This sublayer also hosts most of the meridional circulation jet, as is evident from Fig. 2(b). The innermost sublayer of thickness $\mathrm{Ek}^{2/7}$ is attached to the inside of the TC and mainly serves to continuously connect the azimuthal velocity and its derivative to the interior flow. Finally, the discontinuity in the meridional circulation, also illustrated in Fig. 2(b), is resolved within the inner sublayer of thickness $\mathrm{Ek}^{1/3}$ which is centered around the TC location. Although close agreement of Stewartson's asymptotics with numerical solutions requires lower Ekman numbers [12,13], we found our numerical solutions generally consistent with these scalings. Figures 1(a) and 1(c) show, for example, that Stewartson layer thickness clearly decreases with the Ekman number. Moreover, the inner Ekman boundary layer thickens near the equator where it is expected to scale as $\mathrm{Ek}^{2/5}$ to meet the broader Stewartson layer.

For the moderate Rossby numbers considered in this study ($\mathrm{Ro} \leqslant 0.2$), the hydrodynamical flow solutions remain close to the asymptotic state described above. Figure 2 indeed demonstrates that the interior flow solutions for the largest Rossby numbers explored ($\mathrm{Ro} = 0.2$ at $\mathrm{Ek} = 10^{-4}$ and $\mathrm{Ro} =$

0.03 at $\mathrm{Ek} = 10^{-5}$) are nearly identical to the respective solutions at $\mathrm{Ro} = 2.5 \times 10^{-4}$. For $\mathrm{Ro} \approx 1$, inertial forces become important and cause the development of an equatorial meridional jet which destabilizes the Stewartson layer. In the explored range of Ekman and Rossby numbers, however, the hydrodynamical flow is linearly stable to nonaxisymmetric perturbations [46,47], as we also verified numerically. The onset of the first hydrodynamical nonaxisymmetric Stewartson layer instability occurs, for a given Ekman number, above a certain critical Rossby number Ro_c. Numerical simulations of wide-gap spherical Couette flows similar to those performed in this study show that $\mathrm{Ro}_c \approx 76\,\mathrm{Ek}^{\alpha}$ with $\alpha = 0.63$ [47]. A global linear analysis by Hollerbach [46] reports a similar scaling exponent of $\alpha = 0.65$, and spherical Couette flow experiments by Schaeffer and Cardin [48] are consistent with these numerical results. For the Ekman numbers $\mathrm{Ek} = 10^{-4}$ and 10^{-5} explored here, Ro_c is 0.20 and 0.045, respectively. In the following, we consider only hydrodynamically stable flow solutions with $\mathrm{Ro} < \mathrm{Ro}_c$.

IV. AXISYMMETRIC MAGNETIC SOLUTIONS

We now consider the magnetic case assuming as the initial condition an axial dipole field of strength Lo_0. With this initial condition, the MHD solution remains purely axisymmetric. In Sec. IV A we describe the global flow and field temporal evolution. The field solutions obtained at long times when varying the input model parameters are analyzed in Sec. IV B, where we also discuss the different force balances leading to such solutions.

A. Temporal evolution

The initial dipole field strengths considered in this study are generally small such that $\mathrm{Lo}_0 \ll 1$. In this regime, Lorentz force effects are negligible or rather limited and the flow rapidly approaches the purely hydrodynamical solution described in the preceding section. Toroidal field B_φ can then be generated through the shear across the Stewartson layer. Values of $\mathrm{Lo}_0 \approx 1$ or larger would weaken the internal shear, thus limiting the toroidal field generation.

Figure 3 illustrates the temporal evolution of the kinetic and magnetic energies for the case at $\mathrm{Ek} = 10^{-5}$, $\mathrm{Ro} = 0.03$, $\mathrm{Pm} = 2$, and with an initial dipole field strength of $\mathrm{Lo}_0 = 4.47 \times 10^{-3}$. The initial evolution consists of a transient due to the flow initial condition [Fig. 3(b)] and a growth of the toroidal field B_φ generated by winding the initial dipole field through the internal differential rotation, with the toroidal magnetic energy reaching its maximum in about $270\Delta\Omega^{-1}$ or 9000 system rotations [Fig. 3(d)].

At later times, both field components decay since no dynamo action can occur for a purely axisymmetric field [see Fig. 3(c)]. Pure Ohmic decay is observed at times $t \gtrsim 1500$ when the field largely retains its morphology and its amplitude decreases exponentially on a timescale close to the dipole diffusion time $t_d = r_o^2/\pi^2\eta$ [thin solid line in Fig. 3(c)]. During this phase, the Lorentz force is negligible, so the flow approaches the steady hydrodynamical solution described in Sec. III. For the sake of brevity we refer to this phase of the field evolution as the diffusive phase hereafter. Figures 4(a) and 4(b) show a comparison of the magnetic interior flow solution in the diffusive phase (dotted gray curves) with the respective nonmagnetic one (solid black curves) and demonstrate that the two are indeed indistinguishable.

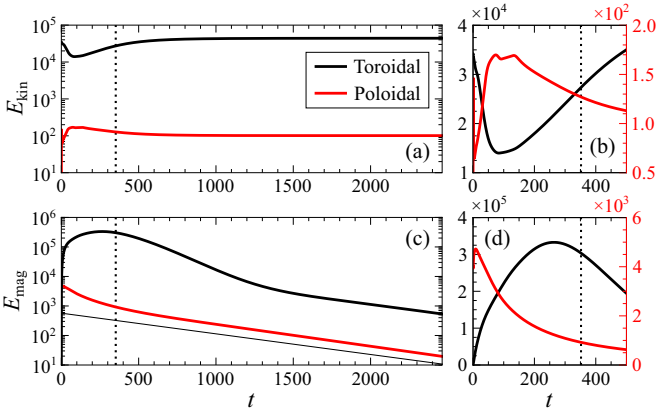

FIG. 3. Temporal evolution of the volume averaged kinetic (E_{kin}) and magnetic (E_{mag}) energies for the axisymmetric case at $\mathrm{Ek} = 10^{-5}$, $\mathrm{Ro} = 0.03$, $\mathrm{Pm} = 2$, and $\mathrm{Lo}_0 = 4.47 \times 10^{-3}$. (a) and (c) display the whole simulation run and (b) and (d) the initial evolution only (note the different scales of the left and right vertical axes). The thin solid line in (c) illustrates the Ohmic decay of a pure dipole field occurring on the timescale $t_d = r_o^2/\pi^2\eta$. The vertical dotted line indicates the time at which nonaxisymmetric perturbations are applied (run Pm2 in Sec. V). Flow and field solutions at this perturbation time are shown in Fig. 4.

An important dimensionless number in this study is the azimuthal Lorentz number

$$\mathrm{Lo}_\varphi = \omega_{\mathrm{A}\varphi}/\Omega, \tag{12}$$

where $\omega_{\mathrm{A}\varphi} = B_\varphi/\sqrt{\rho\mu}d$ is the Alfvén frequency based on the axisymmetric azimuthal field B_φ and $\Omega = \Omega_o + \Omega'$ is the absolute rotation rate. In the diffusive phase where the flow is stationary, the evolution of Lo_φ is determined by B_φ only and this measure can be interpreted as a nondimensional azimuthal field strength.

B. Field solutions during the diffusive phase

We describe here how the axisymmetric field solutions obtained in the diffusive phase depend on the relevant model parameters, namely, the Ekman number Ek, the Rossby number Ro, and the magnetic Prandtl number Pm. A measure which characterizes the toroidal field production, and thus the different solutions obtained, is the toroidal to poloidal field ratio B_φ/B_p. Since both field components decay at about the same rate during the diffusive phase, B_φ/B_p is practically constant during this stage of the field evolution.

Order of magnitude predictions of B_φ/B_p can be obtained by analyzing the relative importance of the different terms in the induction equation. Using the poloidal-toroidal decomposition for an axisymmetric flow

$$\mathbf{u} = \mathbf{u}_p + s\Omega'\hat{\mathbf{e}}_\varphi \tag{13}$$

and magnetic field

$$\mathbf{B} = \mathbf{B}_p + B_\varphi\hat{\mathbf{e}}_\varphi = \nabla \times A\hat{\mathbf{e}}_\varphi + B_\varphi\hat{\mathbf{e}}_\varphi, \tag{14}$$

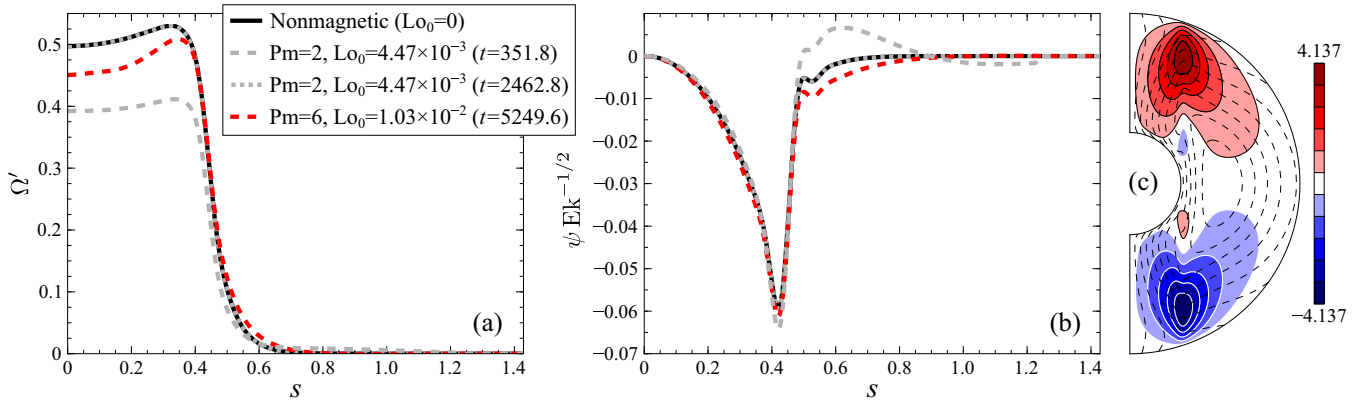

FIG. 4. (a) and (b) Comparison of axisymmetric interior flow solutions between nonmagnetic and magnetic cases at $\mathrm{Ek} = 10^{-5}$ and $\mathrm{Ro} = 0.03$. Solid black curves show the steady nonmagnetic ($\mathrm{Lo}_0 = 0$) solution. Magnetic solutions at $\mathrm{Pm} = 2$ and 6 are illustrated by the gray and red curves, respectively [see the legend in (a) for their Lo_0 values]. Dashed curves display solutions taken at the times t (also given in the legend) when nonaxisymmetric perturbations will be applied. They represent the basic axisymmetric flow configurations of runs Pm2 (dashed gray curves) and Pm6a (dashed red curves) described in Sec. V. Finally, dotted gray curves show the case at $\mathrm{Pm} = 2$ during the diffusive phase of the field evolution (note that the solution is identical to the nonmagnetic one). (c) Magnetic field solution for the case corresponding to the dashed gray curves in (a) and (b). This represents the perturbed axisymmetric field configuration of run Pm2 in Sec. V. Color contours show the axisymmetric azimuthal field B_φ and dashed contour lines the poloidal field.

the induction equation (3) reduces to the scalar equations

$$\frac{\partial A}{\partial t} + \frac{1}{s}(\mathbf{u}_p \cdot \boldsymbol{\nabla})(sA) = \mathrm{Rm}^{-1}(\nabla^2 - s^{-2})A, \quad (15a)$$

$$\frac{\partial B_\varphi}{\partial t} + s(\mathbf{u}_p \cdot \boldsymbol{\nabla})\left(\frac{B_\varphi}{s}\right) = \mathrm{Rm}^{-1}(\nabla^2 - s^{-2})B_\varphi + s(\mathbf{B}_p \cdot \boldsymbol{\nabla})\Omega. \quad (15b)$$

In the above equations, A is the scalar potential which defines the poloidal field $\mathbf{B}_p$ and Ω is the absolute rotation rate defined above. Note that we use the magnetic Reynolds number Rm as the dimensionless parameter here.

The second term on the right-hand side of (15b) is responsible for the toroidal field generation by shearing the poloidal field through the differential rotation, a mechanism commonly referred to as the Ω effect. An estimate for this term is

$$|s(\mathbf{B}_p \cdot \boldsymbol{\nabla})\Omega| \propto B_p, \quad (16)$$

where B_p denotes a characteristic poloidal field amplitude and the differential rotation is taken as the global rotation contrast between the inner and outer boundaries so that $|\nabla\Omega| \approx 1$.

When assuming the shell gap d as a characteristic length scale for the azimuthal field variations and considering $|\mathbf{u}_p| \approx \mathrm{Ek}^{1/2}$ as predicted by Proudman's solution [Eq. (11d)], advection of B_φ by the meridional flow is

$$\left|s(\mathbf{u}_p \cdot \boldsymbol{\nabla})\left(\frac{B_\varphi}{s}\right)\right| \propto \mathrm{Ek}^{1/2} B_\varphi. \quad (17)$$

Under the above assumptions, the diffusion term in (15b) reads

$$\mathrm{Rm}^{-1}|(\nabla^2 - s^{-2})B_\varphi| \propto \mathrm{Rm}^{-1} B_\varphi. \quad (18)$$

The relative contributions of these terms clearly vary with Rm. When $\mathrm{Rm} \ll 1$, magnetic diffusion dominates over the other terms in both the toroidal and poloidal induction equations. When increasing the magnetic Reynolds number to $\mathrm{Rm} \lesssim 1$, the diffusion term (18) may become of the same order of the Ω effect (16). These terms are of $O(1)$ in the Ekman number and therefore largely dominate when compared to the advection scaling (17). In this regime, the expected balance between diffusion and Ω effect yields

$$B_\varphi \propto \mathrm{Rm}\, B_p. \quad (19)$$

Further increasing Rm, advection by the meridional flow starts to be important when $\mathrm{Rm} \approx \mathrm{Ek}^{-1/2}$. Since $\mathrm{Ek} \ll 1$, the Ω effect is expected to be equilibrated by advection and therefore

$$B_\varphi \propto \mathrm{Ek}^{-1/2} B_p. \quad (20)$$

In this regime, B_φ/B_p is independent of Rm and smaller Ekman numbers favor toroidal field generation. For $\mathrm{Rm} \gg \mathrm{Ek}^{-1/2}$, the above scaling relation ceases to be valid. When field advection is the leading term in the force balance, variations of B_φ indeed occur on shorter length scales than those assumed above. Moreover, advection of the poloidal field by the vertical meridional circulation jet within the Stewartson layer also starts to be important.

We verified numerically the above scaling relations calculating $\langle B_\varphi\rangle/\langle B_p\rangle$, the toroidal to poloidal field ratio based on root mean square (rms) volume averages of the respective components. Figure 5 summarizes the results for the explored range of parameters. For $\mathrm{Rm}\,\mathrm{Ek}^{1/2} \lesssim 1$, the simulation data points obey the linear scaling predicted by (19). This regime is referred to as the linear regime hereafter. As expected, deviations from the linear scaling start at $\mathrm{Rm}\,\mathrm{Ek}^{1/2} \approx 1$ and mark the increasingly important role of advection relative to magnetic diffusion. A plateau is then reached when $\mathrm{Rm}\,\mathrm{Ek}^{1/2} \approx 6$. This regime where the toroidal to poloidal field ratio is independent of Rm is compatible with the scaling relation (20) derived above. Hereafter, we refer to this regime as the saturation regime. For $\mathrm{Rm}\,\mathrm{Ek}^{1/2} \gtrsim 10$, $\langle B_\varphi\rangle/\langle B_p\rangle$ first shows a cusp and then increases with a scaling somewhat steeper

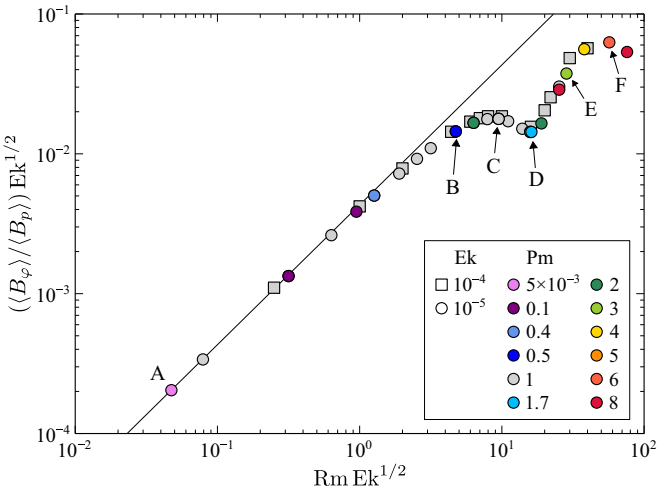

FIG. 5. Scaling of the toroidal to poloidal magnetic field ratio $\langle B_\varphi\rangle/\langle B_p\rangle$ during the diffusive phase of the field evolution with the magnetic Reynolds number Rm. Here angular brackets denote rms volume averages. Squares and circles indicate simulations at the Ekman numbers $\mathrm{Ek} = 10^{-4}$ and 10^{-5}, respectively. The symbol color codes the magnetic Prandtl number Pm (see the legend). The solid black line illustrates the linear scaling $\langle B_\varphi\rangle/\langle B_p\rangle \propto \mathrm{Rm}$ expected for $\mathrm{Rm}\,\mathrm{Ek}^{1/2} \lesssim 1$. Capital letters A–F indicate six cases representative of the different field solutions obtained (see Fig. 6). These cases have Ekman and Rossby numbers $\mathrm{Ek} = 10^{-5}$ and $\mathrm{Ro} = 0.03$, respectively, and different Pm values [case A, $\mathrm{Pm} = 5\times10^{-3}$ (or $\mathrm{Rm} = 15$); case B, $\mathrm{Pm} = 0.5$ (or $\mathrm{Rm} = 1.5\times10^{3}$); case C, $\mathrm{Pm} = 1$ (or $\mathrm{Rm} = 3\times10^{3}$); case D, $\mathrm{Pm} = 1.7$ (or $\mathrm{Rm} = 5.1\times10^{3}$); case E, $\mathrm{Pm} = 3$ (or $\mathrm{Rm} = 9\times10^{3}$); case F, $\mathrm{Pm} = 6$ (or $\mathrm{Rm} = 1.8\times10^{4}$)].

than the linear regime. A second saturation seems to occur at $\mathrm{Rm}\,\mathrm{Ek}^{1/2} \approx 40$.

We also verified that a local measure for the field ratio, namely, B_φ/B_p evaluated at the maximum of the azimuthal field and denoted by $(B_\varphi/B_p)^{\max}$, follows the same scalings discussed above. Here $(B_\varphi/B_p)^{\max}$ is about 120 for the larger Rm cases at $\mathrm{Ek} = 10^{-5}$ shown in Fig. 5 and reveals the strong local dominance of the toroidal field over the poloidal one.

Figure 6 displays typical magnetic field solutions obtained in the different regimes discussed above. The Ekman and Rossby numbers are fixed to $\mathrm{Ek} = 10^{-5}$ and $\mathrm{Ro} = 0.03$, respectively, while the magnetic Reynolds number is varied from $\mathrm{Rm} = 15$ (case A) to $\mathrm{Rm} = 1.8\times10^{4}$ (case F) by increasing the magnetic Prandtl number Pm. All these cases are also marked in Fig. 5. As expected, the field solutions are equatorially antisymmetric. This symmetry is imposed by the purely poloidal initial condition, an axial dipole field, and by the fact that the shear is equatorially symmetric, which gives an equatorially antisymmetric Ω effect.

In the linear regime (case A), the azimuthal field B_φ is characterized by two flux patches largely spread in the fluid domain. The azimuthal field maxima are located within the Stewartson layer where the Ω effect is stronger, i.e., where the poloidal field lines form the largest angles with the cylindrical radial shear. No azimuthal field can be generated near the equator where the poloidal field is mostly vertical and thus $\mathbf{B}_p \cdot \nabla\Omega \approx 0$. In this low-Rm regime, the poloidal field lines are reminiscent of the initial dipolar configuration because advection plays only a marginal role compared to the dominant diffusion.

As can be seen from Fig. 5, a significant departure from the linear regime is observed when increasing Rm to 1.5×10^{3} (case B). The meridional flow now advects B_φ towards the outer boundary and slightly bends the poloidal field lines close to the inner boundary (see Fig. 6). Case C at $\mathrm{Rm} = 3\times10^{3}$ belongs to the saturation regime and presents weak B_φ patches of opposite polarity located close to the inner boundary in each hemisphere. As expected, the Ω effect changes sign in this region since the poloidal field lines are bent radially outwards by the equatorward flow within the inner Ekman boundary layer and the vertical jet within the Stewartson layer.

When further increasing Rm to 5.1×10^{3} (case D), the saturation regime is left and we observe a larger influence of field advection by the meridional flow. Now B_φ lobes of opposite polarity and comparable amplitudes are present in each hemisphere. Finally, advection has a leading role in shaping the field solution at the larger-Rm values of 9×10^{3} (case E) and 1.8×10^{4} (case F). In both cases a single B_φ flux lobe is present in each hemisphere, clearly advected in the direction of the meridional jet. This is particularly evident in case F where these flux lobes are transported towards the outer boundary. The meridional flow also expels the poloidal field out of the Stewartson layer close to the outer boundary. The displaced poloidal flux gets concentrated towards the rotation axis around the polar regions.

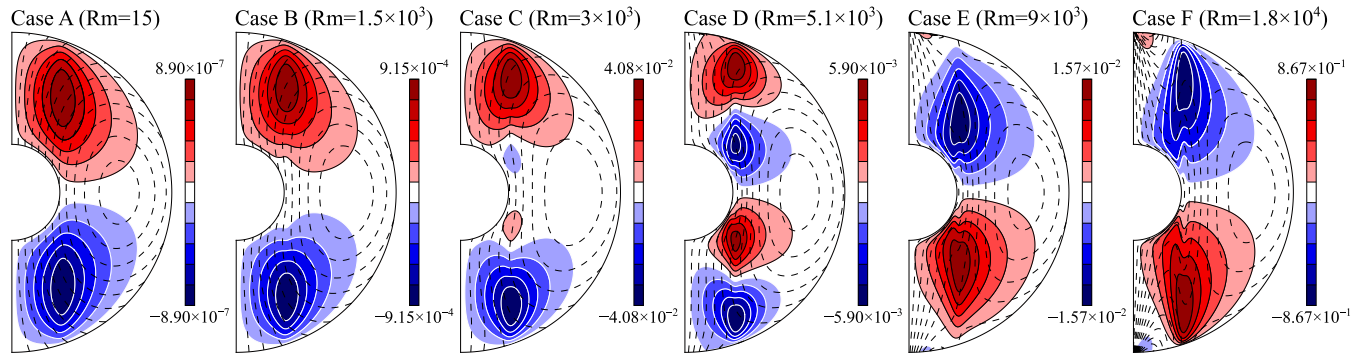

FIG. 6. Axisymmetric magnetic field solutions during the diffusive phase of the field evolution. Color contours show the azimuthal field B_φ and dashed contour lines the poloidal field. The six selected cases (A–F) have different magnetic Reynolds numbers Rm and are representative of the various regimes depicted in Fig. 5. The Ekman number is $\mathrm{Ek} = 10^{-5}$ and the Rossby number $\mathrm{Ro} = 0.03$ in all cases.

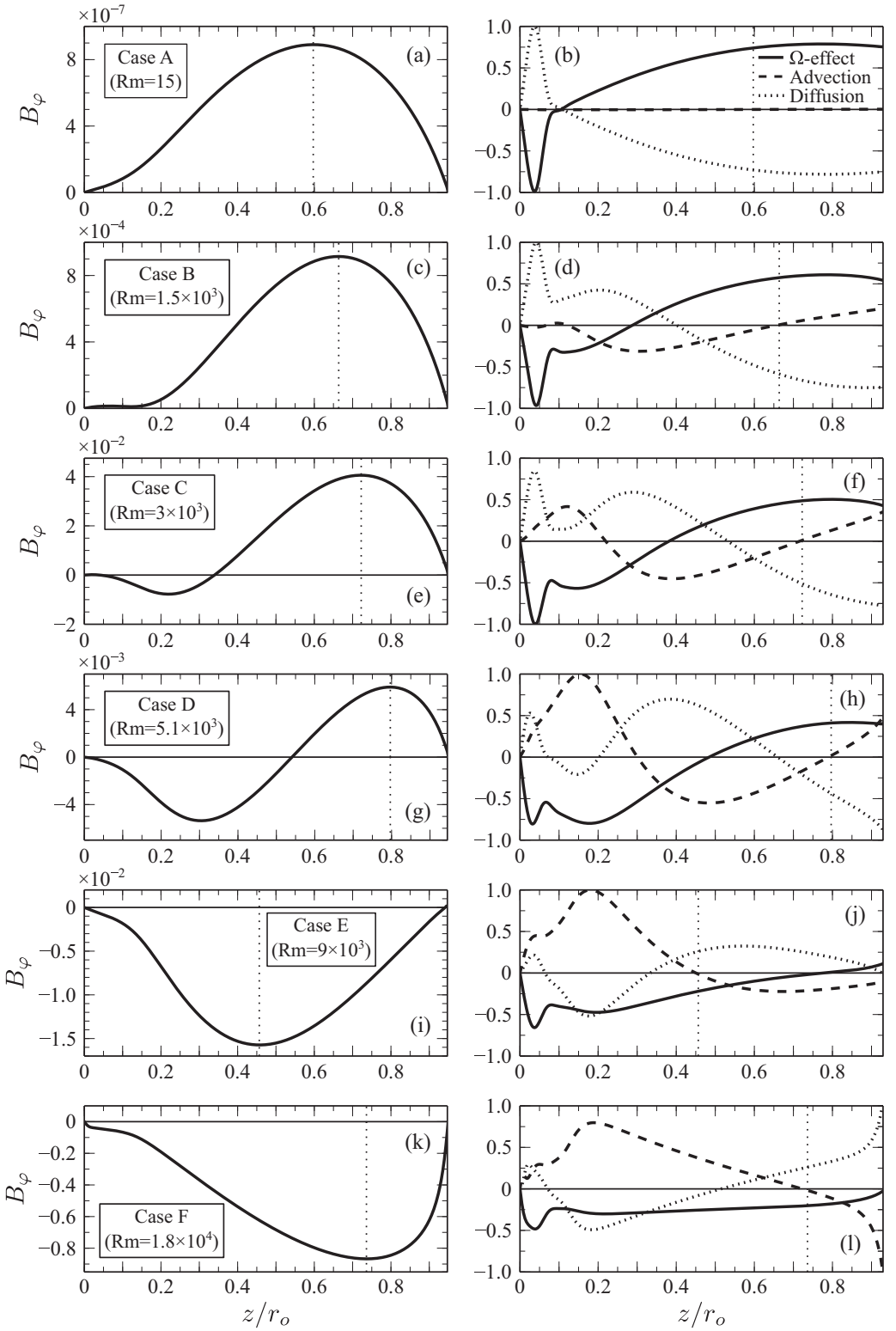

FIG. 7. Force balances for the six axisymmetric field solutions A–F (from top to bottom) shown in Fig. 6. Left and right panels illustrate, respectively, the axisymmetric azimuthal field B_φ and the force terms in the toroidal induction equation (15b) as a function of the vertical coordinate z. These profiles are taken at the cylindrical radius s where $|B_\varphi|$ is maximum and shown for the northern hemisphere ($z > 0$) only. The different force terms [Ω effect, field advection, and magnetic diffusion; see the legend in (b)] are calculated beneath the outer Ekman boundary layer and their amplitude is normalized to the absolute maximum of the forces. The vertical dotted line in each panel indicates the position of the $|B_\varphi|$ maximum.

TABLE I. Selected numerical simulation runs where a nonaxisymmetric instability develops. Columns 2 and 3 list the magnetic Prandtl number Pm and the initial poloidal Lorentz number Lo_0, respectively. The Ekman number is $\mathrm{Ek} = 10^{-5}$ and the Rossby number $\mathrm{Ro} = 0.03$ in all runs. Column 4 details t_{pert}, the time at which the nonaxisymmetric perturbations are introduced. Column 5 lists the maximum azimuthal Lorentz number $\mathrm{Lo}_\varphi^{\mathrm{max}}$ at the perturbation time. Column 6 details the value at the perturbation time of $(B_\varphi/B_p)^{\mathrm{max}}$, the toroidal to poloidal field ratio evaluated at the maximum of B_φ. The last three columns report estimates of the instability drift velocity in the azimuthal direction (c_φ) and in the vertical direction z for the northern ($c_{z>0}$) and southern ($c_{z<0}$) hemispheres.

Run	Pm	Lo_0	t_{pert}	$\mathrm{Lo}_\varphi^{\mathrm{max}}$	$(B_\varphi/B_p)^{\mathrm{max}}$	c_φ	$c_{z>0}$	$c_{z<0}$
Pm2	2	4.47×10^{-3}	351.8	1.84×10^{-2}	60.7	0.118	-1.5×10^{-3}	1.2×10^{-3}
Pm3	3	3.65×10^{-3}	351.9	2.15×10^{-2}	89.4	0.123	-1.8×10^{-3}	2.2×10^{-3}
Pm6a	6	1.03×10^{-2}	5249.6	9.93×10^{-3}	118.7	0.188	-3.6×10^{-3}	3.6×10^{-3}
Pm6b	6	1.03×10^{-2}	6590.9	7.64×10^{-3}	120.3	0.190	-3.5×10^{-3}	3.6×10^{-3}
Pm6c	6	1.03×10^{-2}	7113.6	6.65×10^{-3}	121.6	0.192	-3.2×10^{-3}	3.2×10^{-3}
Pm8b	8	1.03×10^{-2}	8406.3	7.64×10^{-3}	186.5	0.192	-3.9×10^{-3}	3.8×10^{-3}

We verified quantitatively the expected force balances in the six cases discussed above by comparing the different terms in the toroidal induction equation (15b). The right panels of Fig. 7 display the Ω effect, advection, and diffusion terms as a function of the cylindrical vertical coordinate z. These profiles are taken at the cylindrical radius s where $|B_\varphi|$ is maximum. This radius lies within the Stewartson layer and is representative of the global force balance elsewhere in the domain, except for regions in rigid rotation. Since the field is equatorially antisymmetric, only the northern hemisphere ($z > 0$) is shown. The different terms are calculated beneath the outer Ekman layer where they rapidly go to zero due to the insulating boundary condition ($B_\varphi = 0$ at r_o). The respective vertical profiles of B_φ are illustrated in the left panels of the same figure.

In the linear regime of case A, advection of B_φ by the meridional flow is negligible and magnetic diffusion balances the Ω effect as expected [Fig. 7(b)]. Case B deviates from the linear regime and indeed shows a somewhat larger contribution of B_φ advection relative to the other terms [Fig. 7(d)]. In the saturation regime, advection of B_φ becomes comparable in amplitude to the other terms virtually at all locations as predicted above [case C, Fig. 7(f)]. This occurs at the expense of the Ω effect and leads to the saturation of the toroidal field generation. Only at the largest Rm value of case F, a significantly reduced contribution of the Ω effect to the global force balance is observed [Fig. 7(l)] and could explain the second saturation of $\langle B_\varphi \rangle / \langle B_p \rangle$ mentioned before.

In the cases discussed above, the magnetic Reynolds number has been varied by increasing Pm and thus decreasing the relative contribution of magnetic diffusion while leaving the flow solution unchanged. However, Rm can also be varied by increasing the Rossby number Ro for a fixed Pm value. By proceeding this way, we verified that Rm is the key dimensionless parameter which characterizes the different field solutions at long times explored here, in agreement with the scalings shown in Fig. 5.

V. NONAXISYMMETRIC INSTABILITY OF DOMINANTLY AZIMUTHAL FIELDS

In this section we study the stability of the axisymmetric magnetic Couette flow solutions described in the preceding section. For the weak initial dipole field strengths explored ($\mathrm{Lo}_0 \lesssim 10^{-2}$), Lorentz force effects remain small, so the flow is either close or very close to the nonmagnetic solution. The axisymmetric magnetic field then results from the kinematic induction of the initial dipole and, for the large magnetic Reynolds numbers Rm considered, it is dominantly azimuthal. In the following, the Ekman and Rossby numbers will be held fixed at $\mathrm{Ek} = 10^{-5}$ and $\mathrm{Ro} = 0.03$, respectively. As discussed in Sec. III, these Ekman and Rossby numbers ensure that, in the absence of a magnetic field, the flow is stable to nonaxisymmetric perturbations. Thus, any instability will be due to the presence of the magnetic field itself.

Investigating the stability for different magnetic field strengths and magnetic Prandtl numbers, we have found that, for a given value of Pm, the system is unstable above a certain azimuthal field amplitude, measured by the maximum azimuthal Lorentz number in the domain $\mathrm{Lo}_\varphi^{\mathrm{max}}$. The critical value of $\mathrm{Lo}_\varphi^{\mathrm{max}}$ for the instability onset decreases when Pm increases.

In the following we describe a selection of unstable cases, whose control parameters and other relevant measures are listed in Table I. Each run is named following the convention Pmxy, where x is the magnetic Prandtl number value and y a letter that identifies the azimuthal field strength at the perturbation time, as measured by $\mathrm{Lo}_\varphi^{\mathrm{max}}$ (Table I, column 5). Decreasing values of $\mathrm{Lo}_\varphi^{\mathrm{max}}$ are sorted in ascending alphabetical order. To consider different azimuthal field strengths, we use the temporal evolution of the axisymmetric field (Sec. IV A). During the diffusive phase, the flow is stationary and the field decays on the diffusive timescale while conserving its geometry. Then, by introducing the perturbations at successive times, we can indeed study the stability for decreasing strengths of the background azimuthal field. This is done for runs Pm6a, Pm6b, and Pm6c, where the flow closely follows the purely hydrodynamical solution [as demonstrated in Figs. 4(a) and 4(b) for run Pm6a] and the field largely resembles the configuration of case F in Fig. 6. For lower azimuthal field strengths at $\mathrm{Pm} = 6$, namely, $\mathrm{Lo}_\varphi^{\mathrm{max}} \lesssim 5 \times 10^{-3}$, the system is found to be stable. The axisymmetric field configurations of runs Pm6b and Pm8b are similar to each other, and thus the two cases differ only in their magnetic Prandtl number value.

To explore stronger azimuthal magnetic fields, the perturbations have to be introduced earlier in the axisymmetric evolution. This is done for runs Pm2 and Pm3 knowing that at this stage the flow shows some deviations from the purely

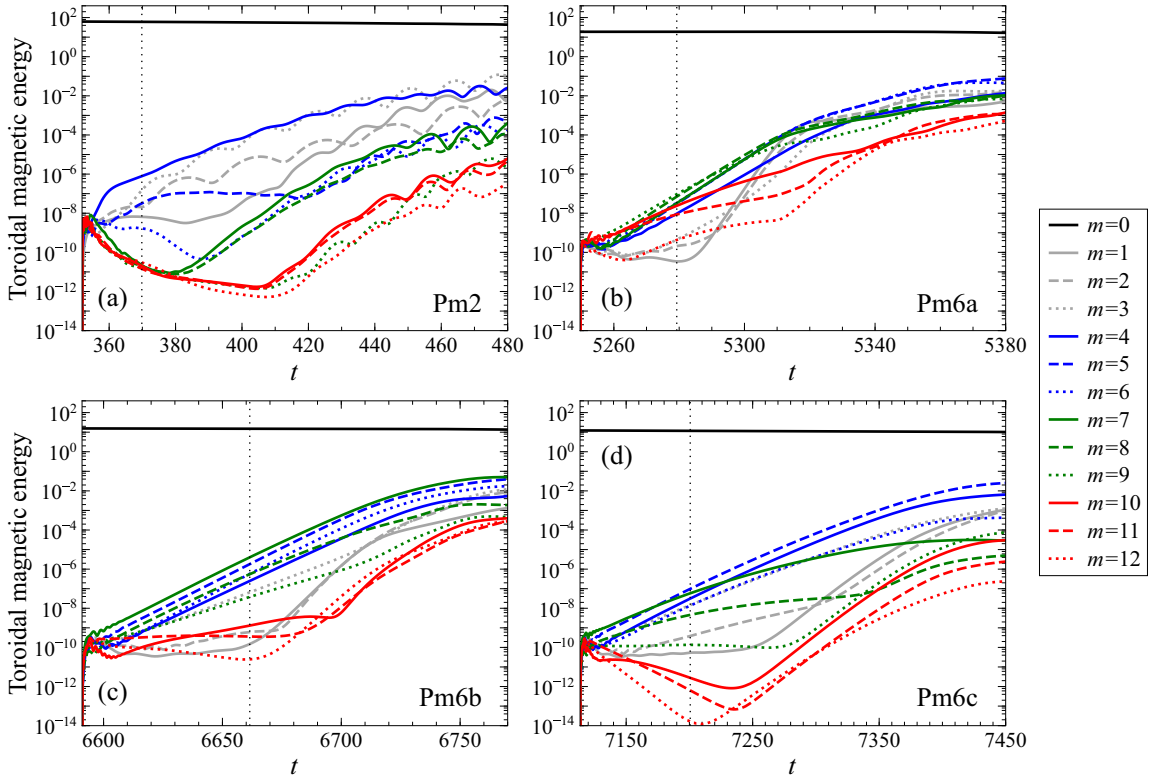

FIG. 8. Temporal evolution of the toroidal magnetic energy of different azimuthal modes m in (a) run Pm2 and (b)–(d) the three runs at Pm = 6. The energy is evaluated as an average over a spherical surface at depth r/r_o roughly located where the axisymmetric azimuthal field is maximum ($r/r_o = 0.8$ and 0.5 for run Pm2 and the three runs at Pm = 6, respectively). Vertical dotted lines indicate the times at which the snapshots of Fig. 9 are taken.

hydrodynamical solution, as demonstrated in Figs. 4(a) and 4(b) for run Pm2, due to a non-negligible role of the Lorentz force. While the temporal evolution of the background axisymmetric fields may in principle modify the instability development, we will see that this is not the case in our numerical simulations because the most unstable modes grow on a timescale much shorter than the evolution timescale of the background fields.

Another important property of the background axisymmetric field is that it is always strongly dominated by the toroidal component. The local ratio $(B_\varphi/B_p)^{\max}$, listed in column 6 of Table I, is indeed of about 120 for the runs at Pm = 6 and reaches more than 180 for run Pm8b. Runs Pm2 and Pm3 have smaller values of about 60 and 90, respectively.

The applied perturbation consists of a nonaxisymmetric random poloidal field for all spherical harmonic degrees $\ell > 0$ and orders $m > 0$. We choose the noise amplitude to be several orders of magnitude smaller than the maximum axisymmetric field strength. Within few system rotations after the perturbation time, a nonaxisymmetric instability starts to grow in all the selected runs. Figure 8 displays the temporal evolution of the toroidal magnetic energy of the first 13 azimuthal modes m in runs Pm2, Pm6a, Pm6b, and Pm6c. As mentioned above, the axisymmetric field ($m = 0$) is practically stationary on the typical timescale of the instability growth. The linearly unstable modes are $m \leqslant 6$ for run Pm2, $m \leqslant 14$ for Pm6a, $m \leqslant 11$ for Pm6b, and $m \leqslant 9$ for Pm6c. Higher azimuthal modes in each run are initially subcritical and grow only at later times due to nonlinear mode energy transfers. In run Pm6a, for example, the nonlinear phase is reached after a period of roughly $40\Delta\Omega^{-1}$ from the perturbation time [see Fig. 8(b)]. At this stage we find that the ratio of the nonaxisymmetric magnetic energy to the axisymmetric one becomes of order unity at the locations where the instability develops. Interestingly, the nonlinear growth of $m = 1$ and $m = 2$ is significantly faster than the linear one, presumably because of mode interactions between the faster growing linear modes. The most unstable linear mode is $m_{\max} = 5$ in runs Pm6a and Pm6c and $m_{\max} = 6$ in run Pm6b. The growth rate of these modes lowers when $\mathrm{Lo}_\varphi^{\max}$ decreases. Unstable linear modes in runs Pm2 and Pm3 have relatively large growth rates. We will interpret these results using predictions from a local linear stability analysis in Sec. VI B.

Figure 9 presents the spatial distribution of the instability during the linear phase of its growth. Left and right panels display, respectively, map projections and meridional sections of the total nonaxisymmetric azimuthal field B'_φ. The instability clearly develops over the Stewartson layer and is confined in regions around and below the axisymmetric $|B_\varphi|$ maximum, as can be seen by comparing the axisymmetric field solutions displayed in Figs. 4(c) and 6 (case F) for run Pm2 and the runs at Pm = 6, respectively. The characteristic length scale of the instability in the meridional plane is comparable to the Stewartson layer thickness, while the azimuthal length scale $\lambda_\varphi \approx 2\pi r_i/m_{\max}$ is a few times larger in all the cases considered.

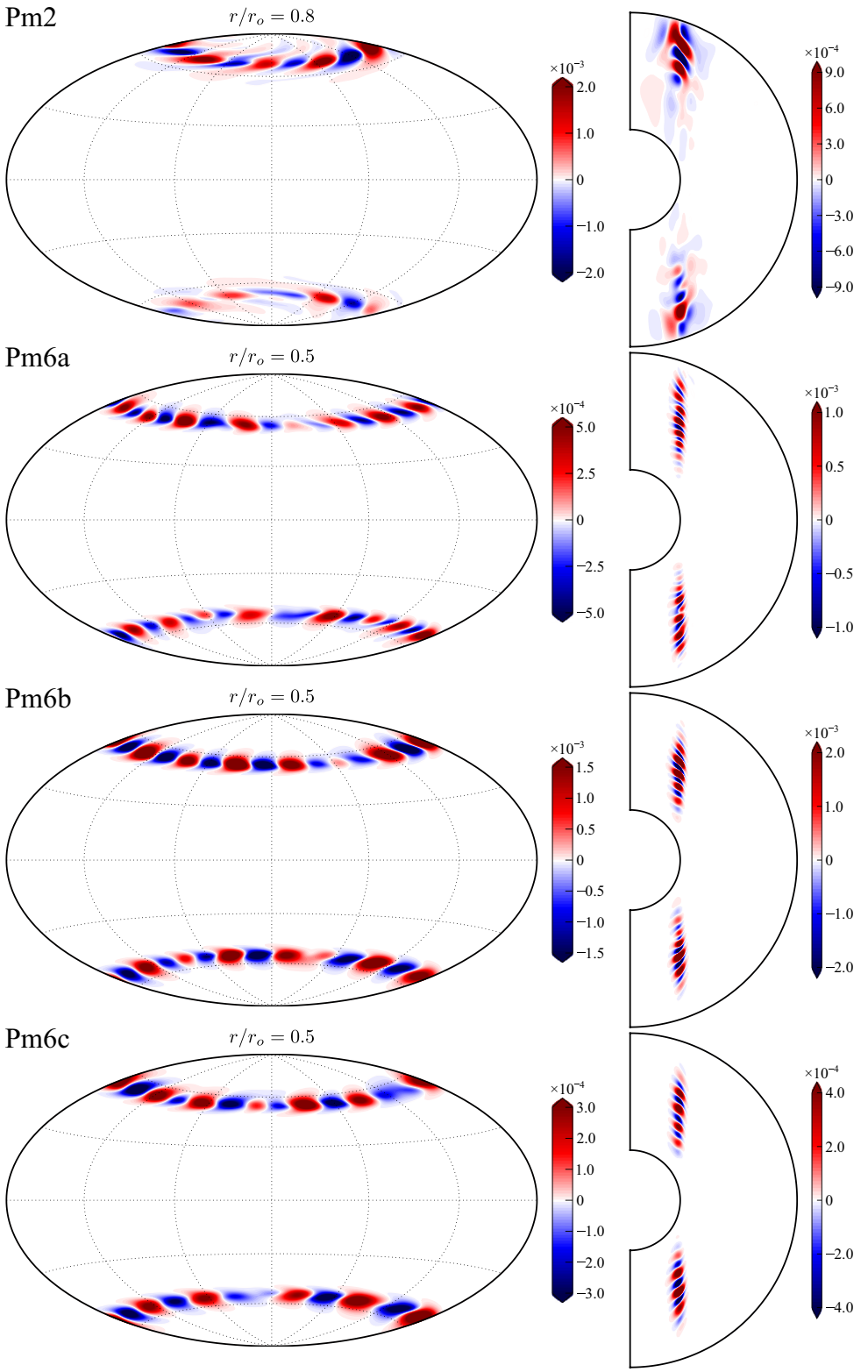

FIG. 9. Nonaxisymmetric instability during the linear phase of its growth. Runs Pm2, Pm6a, Pm6b, and Pm6c are shown from top to bottom. Left and right panels display, respectively, map projections and meridional sections of the total nonaxisymmetric azimuthal field B'_φ. The map projections are taken at depths r/r_o indicated on top of each panel. These snapshots are taken at the times displayed in the magnetic energy evolution of Fig. 8.

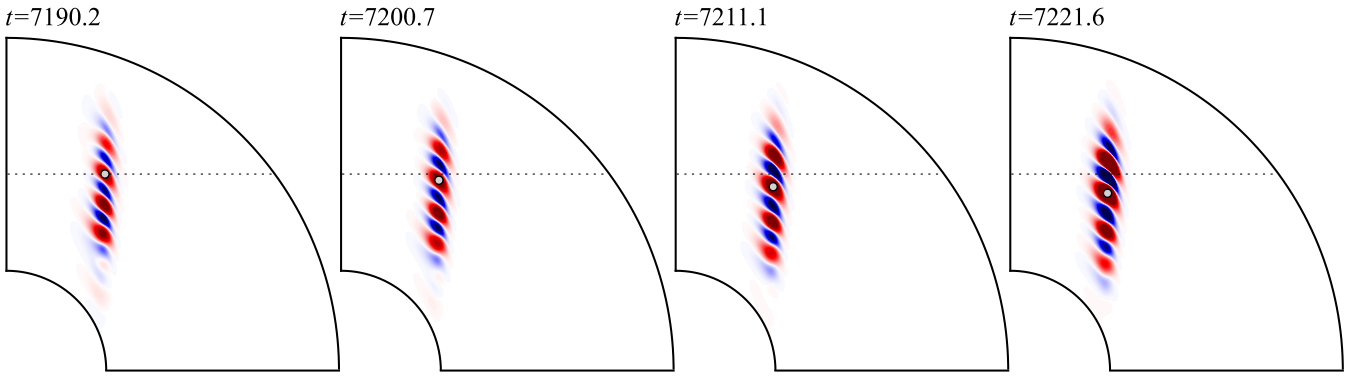

FIG. 10. Meridional sections (northern hemisphere only) showing the temporal evolution of the total nonaxisymmetric azimuthal field B'_φ in run Pm6c. The instability drifts in the vertical direction towards the inner boundary at constant velocity and with a mostly fixed wave packet structure. The gray dot marks the position of a mode crest. The initial vertical position of this crest is indicated by the horizontal dotted line, which can be used as a reference to track the slow instability motion.

We observe that the instability drifts azimuthally in the prograde direction. This drift occurs at an intermediate rate between Ω_o and $\Omega_o + \Delta\Omega/2$, which is compatible with the characteristic mean flow rotations within the Stewartson layer (see Table I, column 7 for values of the azimuthal drift velocity c_φ in all runs explored). While drifting in the azimuth, the perturbations also propagate vertically towards the inner boundary, namely in the $-\hat{\mathbf{e}}_z$ and $+\hat{\mathbf{e}}_z$ directions in the northern and southern hemispheres, respectively, with a mostly fixed wave packet structure (see Fig. 10). Vertical drift velocities in the two hemispheres, also reported in Table I, are low in magnitude, with values typically two orders of magnitude smaller than those of c_φ. When approaching the inner boundary, the instability structures vanish at the intersection between the Stewartson layer and the inner Ekman layer where viscous effects are important.

VI. INTERPRETATION OF THE INSTABILITY

Having described the nonaxisymmetric instability observed in the numerical simulations, we now closely analyze and interpret its properties. The instability nature is characterized in the following section where we provide evidence in favor of the MRI. The observed growth rates and unstable locations are then compared with predictions obtained from a local linear stability analysis in Sec. VI B.

A. Evidence for nonaxisymmetric MRI

In the following we argue that the instability found in our numerical simulations is of the magnetorotational type. In the magnetic Couette flow considered in this study, the free energy available for an instability to develop comes either from the shear or from the magnetic field. Hydrodynamically stable shear flows, like the one we are considering, can become magnetohydrodynamically unstable through the MRI. In this instability the magnetic field acts only as a catalyst, enabling the kinetic energy of the shear to be drawn in. Purely magnetic instabilities, possibly affected by the flow, can also be triggered. For our magnetic configurations largely dominated by the toroidal component, the most likely is the so-called Tayler instability (TI) [49–51], which is a pinch-type instability of purely axisymmetric toroidal fields with $m = 1$ the fastest growing mode.

The first indication in favor of the MRI is that the instability we observe clearly develops where the shear is located, that is, on the Stewartson layer. A distinct property of MRI in the presence of azimuthal fields is its traveling wave nature. An azimuthal drift of nonaxisymmetric MRI modes is expected both for purely azimuthal and for combined vertical and azimuthal (helical) field configurations [29,52–54]. In the presence of helical fields, MRI modes also propagate along the vertical coordinate z. These oscillatory solutions, predicted by Taylor-Couette stability studies [26,32] and also observed experimentally [55–57], arise due to a break of the reflectional symmetry in z introduced when considering a helical field. The direction of propagation (parallel or antiparallel to the rotation axis direction $\hat{\mathbf{e}}_z$) is determined by the handedness of the magnetic field (left handed or right handed, respectively). The characteristic vertical drift rate is small, typically tens of times lower than the mean flow rotation rate. In a spherical geometry, Petitdemange *et al.* [35] confirmed the slow traveling wave nature of MRI in a helical field, for both axisymmetric and nonaxisymmetric perturbations.

In our numerical simulations, which consider mixed poloidal and toroidal background field configurations, the instability drifts at constant velocities in both the azimuthal and vertical directions as expected. The azimuthal drift is prograde and vertically the instability propagates towards the inner boundary, namely, in the $-\hat{\mathbf{e}}_z$ and $+\hat{\mathbf{e}}_z$ directions in the northern and southern hemispheres, respectively. This opposite propagation direction in z is due to the different handedness of the background axisymmetric field in the two hemispheres. In agreement with the above-mentioned findings, the vertical drift rates are low, typically four orders of magnitude smaller than the mean flow rotation rate.

Another property of the MRI is that it is much favored when the mean angular velocity Ω decreases radially outwards [23,58]. We tested this property in our simulations by slowing down the inner boundary rotation rate during the linear phase of the instability growth. As we invert the sign of the radial angular velocity gradient such that $\mathrm{Ro} = -0.03$, all the unstable modes quickly become subcritical.

As discussed by Jouve *et al.* [59], a key parameter to distinguish between the MRI and the TI is the azimuthal Lorentz number Lo_φ defined in Eq. (12). Large values of Lo_φ favor the TI since the strong magnetic tension resists shear-induced field modifications required by the MRI. In our numerical simulations, Lo_φ is always small at the times when the axisymmetric solutions are perturbed. Values of $\mathrm{Lo}_\varphi^{\max}$ are indeed of about 10^{-2} or lower in all the explored runs (Table I, column 5). Moreover, as expected in this MRI regime, the most unstable azimuthal modes are $m > 1$ in our numerical simulations. Modes $m > 1$ may also be excited by the TI but only in regions where the latitudinal gradients $\partial B_\varphi^2/\partial\theta$ are positive and large [50]. In the axisymmetric field configurations explored, these regions lie mainly outside the Stewartson layer where the simulations show no unstable behavior. To conclude, all the above observations strongly support the MRI as the instability being triggered in our numerical simulations.

B. Comparison with local linear stability analysis

Nonaxisymmetric MRI induced by toroidal fields has been investigated in different contexts, from stellar accretion disks (see [60,61] for reviews on the subject) to laboratory experiments [30,55,57], using different types of approximations and simplified flow configurations (e.g., [60,62,63]). For our case, a global linear analysis would require us to solve a two-dimensional boundary value problem because of the complex geometry of the background flow and magnetic field. The shearing coordinates formalism, employed, for example, by Balbus and Hawley [24] or by Petitdemange *et al.* [35], would be complicated to apply here for the same reason. In addition, this latter framework provides transient exponential growths of the unstable modes that are not directly comparable to those found in the present simulations. To further analyze our numerical results, we instead resort to the local linear stability analysis of Acheson [40].

Acheson studied the stability of a purely axisymmetric toroidal field B_φ in a differentially rotating, stably stratified Boussinesq fluid of uniform viscosity, thermal conductivity, and magnetic diffusivity. The local linear analysis is performed in cylindrical coordinates (s, φ, z) and assumes harmonic perturbations in space and time of the form $\exp[i(k_s s + k_z z + m\varphi - \sigma t)]$. Here k_s and k_z denote the radial and vertical wave numbers, respectively. The rate at which the perturbations grow (or decay) is determined by $\gamma = \mathrm{Im}(\sigma)$. These perturbations are of small amplitude and have small length scales compared to the characteristic scales of variation of the background flow and field configurations. Solutions of the linearized MHD equations proportional to the above ansatz then satisfy a dispersion relation further simplified by assuming azimuthal perturbation wavelengths much larger than the meridional ones, namely, $k_\varphi^2 \ll k_s^2 + k_z^2$, where $k_\varphi = m/s$ is the azimuthal wave number.

The resulting dispersion relation, adapted to our setup where no buoyancy is present, is examined in the Appendix. For the discussion here it suffices to know that, when scaling σ with the local rotation rate Ω such that $\tilde{\sigma} = \sigma/\Omega$, the dispersion relation is a function f that satisfies the condition $f(\tilde{\sigma}, m, \beta, q, b, L_o, R_e, R_m) = 0$. In addition to the azimuthal order m, the dimensionless parameters entering this relation are the poloidal wave number ratio

$$\beta = k_s/k_z, \tag{21a}$$

the shear parameter

$$q = \frac{\partial \ln \Omega}{\partial \ln s} - \beta \frac{s}{z}\frac{\partial \ln \Omega}{\partial \ln z}, \tag{21b}$$

a parameter related to the azimuthal field derivatives

$$b = \frac{1}{2}\left(\frac{\partial \ln B_\varphi^2}{\partial \ln s} - \beta \frac{s}{z}\frac{\partial \ln B_\varphi^2}{\partial \ln z}\right), \tag{21c}$$

the (local) azimuthal Lorentz number

$$L_o = \omega_\mathrm{A}/\Omega, \tag{21d}$$

with $\omega_\mathrm{A} = B_\varphi/\sqrt{\mu\rho}s$, and finally the hydrodynamical and magnetic Reynolds numbers

$$R_e = \frac{\Omega}{\nu k^2} \quad \text{and} \tag{21e}$$

$$R_m = \frac{\Omega}{\eta k^2}, \tag{21f}$$

where $k^2 = k_s^2 + k_z^2$. The Reynolds numbers are related by $R_m/R_e = \mathrm{Pm}$.

In the following we will use this dispersion relation in two ways. First, we compute growth rates (the imaginary part of $\tilde{\sigma}$, or equivalently γ/Ω) of the most unstable azimuthal modes $m_{\max}$ observed in the numerical simulations at each point of the meridional plane. This is done by calculating the local values of the above dimensionless parameters in the meridional plane from the axisymmetric configurations perturbed. Locations of positive growth rates determine an unstable region that we then compare with the amplitude of the unstable azimuthal modes $m > 0$ observed in the simulations. Second, by estimating meridional averages of the dispersion relation parameters from the axisymmetric simulations, we compute the growth rate of each mode m, which we then compare with the values directly derived from the simulations.

In both cases, the poloidal wave number ratio β needs to be estimated and this is done from the numerical simulation results by evaluating typical length scales of the instability in the s and z directions during the linear phase of its growth. To determine these length scales, and according to the meridional distribution of the instability displayed in Fig. 9, the following algorithm has been employed. Consider a meridional section at the azimuthal numerical grid point φ_i. The relative maxima of $|B'_\varphi|$ are identified. For each of these maxima, we then calculate the full width at half maximum in the s and z directions. Their arithmetic means give the length scale estimates $\lambda_s^{(i)}$ and $\lambda_z^{(i)}$. This procedure is repeated for each of the N_φ azimuthal grid points, and the arithmetic means $\overline{\lambda}_s = N_\varphi^{-1}\sum_{i=1}^{N_\varphi}\lambda_s^{(i)}$ and $\overline{\lambda}_z = N_\varphi^{-1}\sum_{i=1}^{N_\varphi}\lambda_z^{(i)}$ finally provide the estimate $\beta = \overline{\lambda}_z/\overline{\lambda}_s$. Values of $\overline{\lambda}_s$ and $\overline{\lambda}_z$ are listed in Table II (columns 2 and 3) for all runs explored. As mentioned in the preceding section,

TABLE II. Estimates of the instability length scales and of the dispersion relation parameters for the simulation runs explored. Columns 2 and 3 list $\bar{\lambda}_s$ and $\bar{\lambda}_z$, the characteristic instability length scales in the cylindrical radial and vertical directions respectively. Column 4 details the poloidal wave number ratio estimate $\beta = \bar{\lambda}_z/\bar{\lambda}_s$. Columns 5–9 report meridional averages of the dimensionless parameters entering the dispersion relation and defined in Eqs. (21b)–(21f). See the main text for further explanation.

Run	$\bar{\lambda}_s/d$	$\bar{\lambda}_z/d$	β	$\langle q\rangle$	$\langle b\rangle$	$\langle L_o\rangle$	$\langle R_e\rangle$	$\langle R_m\rangle$
Pm2	0.058	0.086	1.54	−0.047	−0.63	0.027	222.6	445.2
Pm3	0.055	0.069	1.26	−0.050	−1.40	0.030	184.7	554.1
Pm6a	0.036	0.042	1.17	−0.052	−1.57	−0.015	74.7	448.2
Pm6b	0.038	0.042	1.11	−0.049	−1.07	−0.012	79.4	476.4
Pm6c	0.042	0.047	1.12	−0.047	−0.89	−0.011	97.1	582.6
Pm8b	0.032	0.040	1.25	−0.046	−1.47	−0.012	62.9	503.2

these length scales are generally comparable to the Stewartson layer thickness $\delta_S/d \sim \mathrm{Ek}^{1/4} \approx 0.056$, although moderately smaller in the larger-Pm runs. Vertical length scales $\bar{\lambda}_z$ are mildly larger than the radial ones in all runs analyzed. These estimates are also used to evaluate the meridional wave number entering R_e and R_m as $k^2 = 1/\bar{\lambda}_s^2 + 1/\bar{\lambda}_z^2$.

After determining β, we calculate the unstable fluid regions predicted by the local dispersion relation for our axisymmetric configurations as described above. The theoretical predictions obtained for runs Pm2 and Pm6a are compared with the respective numerical simulation results in Fig. 11. Black contour lines display the predicted growth rates for the most unstable azimuthal mode $m_{\max}$ observed in each simulation. Because of the equatorial symmetry of the problem, we evaluate these growth rates in the northern hemisphere only. Figure 11 demonstrates that the predicted unstable regions correlate well with the observed instability locations. We found similar good agreement when analyzing the other runs and we therefore do not present the results here.

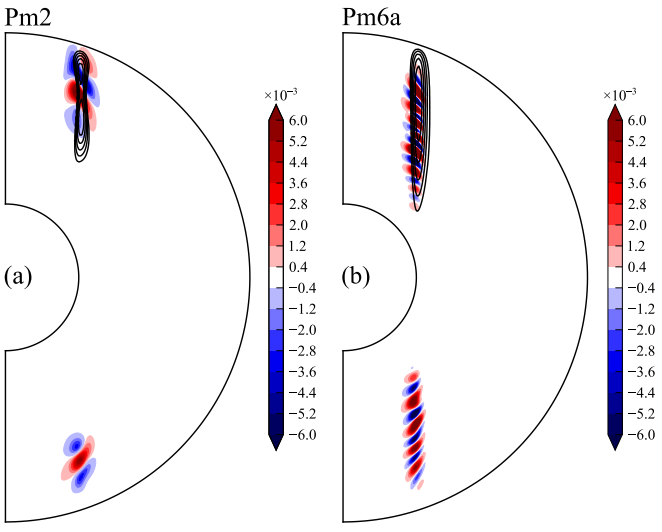

FIG. 11. Comparison of the unstable regions predicted by the local dispersion relation with the numerical simulation results. Meridional sections of the total nonaxisymmetric azimuthal field B'_φ during the linear phase of the instability growth are shown for runs (a) Pm2 and (b) Pm6a. Black contour lines in the northern hemisphere display the growth rates $\gamma/\Omega > 0$ predicted by the local dispersion relation for the most unstable azimuthal mode $m_{\max}$ observed in the simulation ($m_{\max} = 4$ and 5 for runs Pm2 and Pm6a, respectively).

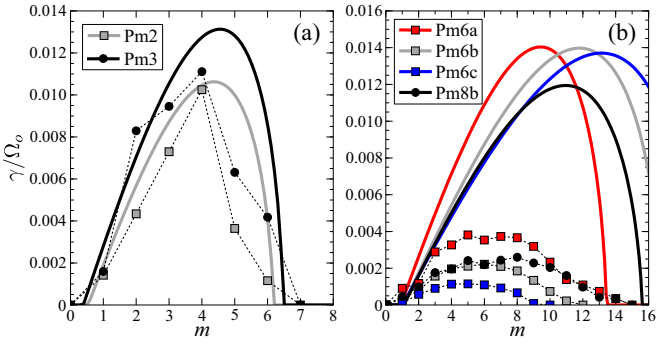

FIG. 12. Comparison of the growth rates γ/Ω_o of the unstable azimuthal modes m observed in the numerical simulations (data points) with those predicted by the local dispersion relation (solid curves). The theoretical predictions are obtained with the estimates of the dispersion relation parameters listed in Table II (see the main text for further details). (a) Runs Pm2 and Pm3 show good agreement with the theoretical growth rates, whereas (b) runs at Pm = 6 and 8 present larger deviations.

How does the growth rate of each unstable azimuthal mode observed in the numerical simulations comply with the theoretical predictions? Figure 12 displays the growth rates of the linearly unstable modes m in all the explored runs. These are evaluated from the toroidal magnetic energy evolution of each mode (see Fig. 8 for run Pm2 and the three runs at Pm = 6). For a comparison with the local linear theory, as already anticipated above, we have to evaluate meridional averages of the dispersion relation parameters (21b)–(21f). These averages are calculated over an unstable region whose boundaries are specified as follows. Because of the equatorial symmetry of the problem, only the northern hemisphere ($z > 0$) is considered. In the cylindrical radial direction s, the unstable region is bound by $r_i - \bar{\lambda}_s/2$ and $r_i + \bar{\lambda}_s/2$. In the vertical direction z, we exclude the upper Ekman boundary layer and the lower bound is adjusted so that the averages do not depend strongly on its precise location. We denote these meridional averages by the angular brackets hereafter, and we report the values obtained for each run in Table II. These values are used to calculate the theoretical growth rates shown in Fig. 12 as solid curves.

Runs Pm2 and Pm3, displayed in Fig. 12(a), show good agreement with the theoretical predictions for modes $m \leqslant 4$, whereas higher unstable modes deviate more significantly. Growth rates observed for the runs in the diffusive phase instead differ considerably from the predicted ones for all m [Fig. 12(b)]. The most unstable modes $m_{\max}$ observed in the numerical simulations are also systematically smaller than those predicted by the local linear theory. In runs at Pm = 6, for example, $m_{\max}$ seems to decrease when decreasing the azimuthal Lorentz number, whereas the linear theory shows the opposite behavior. In the following section we discuss how the linear theory can become less accurate in predicting the growth rates in these latter cases.

Validity of linear analysis assumptions

To explain the observed differences with the predictions obtained from the local linear analysis of Acheson, we now discuss in detail the validity of its assumptions and their limitations for our numerical simulations. First, we consider the short-wavelength approximation which requires that the meridional wavelength of the perturbations is locally much smaller than the scale heights of the background axisymmetric configuration. As detailed in the Appendix, we have compared the characteristic meridional instability length scale with the typical scales of variation of the axisymmetric flow and field solutions and concluded that the short-wavelength approximation is not violated. The assumption that the azimuthal wavelength of the perturbations is much larger than the meridional one is also marginally true. In fact, the characteristic azimuthal length scale of the instability is typically 3 or 4 times larger than the meridional one in all the explored runs.

This last assumption, however, imposes additional limitations that are evident when adopting shearing coordinates, i.e., a Lagrangian reference frame locally corotating with the fluid. In shearing coordinates, the radial wave number is time dependent (see, e.g., [24])

$$k_s(t) = k_s' - m\frac{d\Omega}{ds}t = k_s' - k_\varphi \frac{s}{H_\Omega}\Omega t. \tag{22}$$

Here k_s' denotes the unsheared radial wave number in the Lagrangian frame, $k_\varphi = m/s$ the azimuthal wave number, and $H_\Omega = |\Omega\,(d\Omega/ds)^{-1}|$ the scale height of the mean angular velocity. Equation (22) is valid for a vertically invariant flow, a well satisfied assumption in our numerical simulations. For axisymmetric perturbations ($m = 0$), k_s does not vary in time. In the analysis of Acheson, the time-dependent term is also neglected for nonaxisymmetric perturbations. This is motivated by the fact that, for times t smaller than the local rotation period Ω^{-1}, since $s/H_\Omega \lesssim O(1)$, then $k_s(t) \approx k_s'$. Should $t \gg \Omega^{-1}$, however, shearing effects on the radial wave number may be important and modify the instability evolution. A transient amplification of nonaxisymmetric modes, i.e., a rapid growth occurring only for a finite period of time, is indeed to be expected in this formalism [24,35]. Enhanced viscous and diffusive effects acting on the small-scale sheared modes could eventually further stabilize the system. The larger magnetic tension of these sheared modes may also work as an additional stabilizing effect.

In our numerical simulations, the separation between the characteristic azimuthal and radial wavelengths of the instability is not large and shearing effects may then play a role during the linear phase of the instability growth. The question then naturally arises as to what the critical azimuthal mode m_S is for which these effects start to impact on the unstable wave numbers. According to Eq. (22), the radial wave number variations expected in a period t since the initial instability growth at $t = 0$ are such that

$$\Delta k_s(t) = |k_s(t)| - |k_s(0)| \leqslant |m|\left|\frac{d\Omega}{ds}\right| t. \tag{23}$$

Here we used the fact that the instability drifts in the prograde direction and therefore $m = |m|$. During the e-folding time of the most unstable azimuthal mode $\gamma_{\max}^{-1}$, we consider these variations significant when

$$\Delta k_s\left(\gamma_{\max}^{-1}\right) \geqslant |k_s(0)|, \tag{24}$$

which yields

$$|m| \geqslant |k_s(0)||d\Omega/ds|^{-1}\gamma_{\max}. \tag{25}$$

The critical mode m_S is then defined by the equals sign in the above condition. Using $|k_s(0)| \approx 1/\overline{\lambda}_s$ and taking for $|d\Omega/ds|$ its meridional average in the unstable region, we obtain the estimate

$$m_S \approx \gamma_{\max}/\left(\overline{\lambda}_s\langle|d\Omega/ds|\rangle\right), \tag{26}$$

where $\gamma_{\max}$ is the growth rate of the most unstable mode predicted by the dispersion relation (see also Fig. 12).

For runs Pm2 and Pm3, $m_S \approx 2$, which can be compatible with the deviations from the predicted growth rates observed for modes $m > 4$ [Fig. 12(a)]. Similar values of $m_S \approx 3$ are obtained for the runs at Pm = 6 and 8, which however show significant discrepancies with the predicted growth rates for all azimuthal modes. Nevertheless, since higher modes m are expected to be favored in these latter runs, shearing effects are likely to be more important compared to the cases at low Pm. Viscous diffusion may also be more efficient at larger Pm to damp the small-scale sheared modes. These observations are consistent with the behavior shown by the runs at Pm = 6 and clearly seen in Fig. 12(b): The larger the most unstable azimuthal mode predicted by the dispersion relation, the smaller the one observed in the numerical simulations.

VII. SUMMARY AND DISCUSSION

Magnetic fields and differential rotation are almost ubiquitous in the interior of planets and stars. The study of differentially rotating flows in the presence of magnetic fields thus assumes particular relevance in astrophysics. Magnetic spherical Couette flow is a prototype of such a problem where the differential rotation is forced mechanically via the boundaries. This idealized setup has the additional advantages that it is prone to analytical treatment and can be realized in laboratory experiments.

Previous numerical studies of magnetic spherical Couette flow mostly considered imposed magnetic fields with relatively simple topologies (e.g., [16,33–35,64]). Whereas these studies have direct applications to interpret the results of laboratory experiments where magnetic fields are externally imposed, this approach falls short on astrophysical situations where the field freely evolves in time. Moreover, these studies often explored regimes where the flow is hydrodynamically unstable [19,36]. In this work we have instead investigated numerically the basic states and the stability of a magnetic spherical Couette flow where the field evolves self-consistently from an initial dipolar configuration, focusing on the regime of fast outer boundary rotations and slight boundary differential rotations which is hydrodynamically stable. This allowed us to examine instabilities which are entirely due to the presence of a magnetic field.

In our numerical simulations the axisymmetric toroidal field B_φ is produced by winding the poloidal field through the shear within the Stewartson layer. A variety of axisymmetric field solutions is obtained depending on the importance of

field advection relative to magnetic diffusion, which is quantified by the magnetic Reynolds number Rm. Our numerical simulations show that the efficiency of the toroidal field generation saturates when field advection becomes of leading order in the force balance, namely, for $6 < \mathrm{Rm}\,\mathrm{Ek}^{1/2} < 10$, and then increases again for larger values of Rm.

We have then examined the stability of some of these axisymmetric solutions, focusing on the dominantly toroidal field configurations obtained for $\mathrm{Rm} \geqslant 6 \times 10^3$. We have found that a nonaxisymmetric instability develops when a certain azimuthal field strength (measured by the azimuthal Lorentz number Lo_φ) is exceeded. The critical value of Lo_φ for the instability onset decreases when the magnetic Prandtl number Pm increases.

We argue that the instability found in our numerical simulations is of the magnetorotational type. As expected for the MRI, the instability develops in regions where the shear is present, that is, on the Stewartson layer, and only when the mean rotation rate decreases radially outwards.

It is well known that linearly unstable MRI modes arise as traveling waves in the presence of helical, thus mixed poloidal and toroidal, magnetic field configurations [29,32,52,57]. In particular, nonaxisymmetric modes are expected to drift azimuthally at a rate comparable to the mean flow rotation rate and in the vertical direction with a significantly slower rate. Compatibly with such properties, the instability observed in our numerical simulations drifts azimuthally in the prograde direction and vertically towards the inner shell boundary. The azimuthal drift occurs at rates truly comparable with the mean flow rotations within the Stewartson layer, and drift rates in the vertical direction are a few orders of magnitude smaller.

Similarly to what has been explored here, Petitdemange *et al.* [35] studied the development of nonaxisymmetric MRI modes in a spherical shell imposing a cylindrical radial shear and a helical magnetic field. Although the authors focused on the magnetostrophic regime, which is different from the regime considered in this study, we note that the spatial distribution of the unstable modes is nevertheless remarkably similar to the one obtained here.

Linear analyses of the MHD equations can be used to study and characterize the instability in further detail. They can be performed using different types of approximations, from fully global to local approaches. Global linear analyses (e.g., [25,65]) could provide a close description of the unstable modes in our numerical simulations, but they are certainly not straightforward to apply. A local approach often employed to describe nonaxisymmetric modes considers shearing coordinates, namely, a reference frame locally corotating with the mean flow (see, e.g., [24,35]). In this formalism only transient amplification of the unstable modes is possible, and results from direct numerical simulations are consequently difficult to compare. Such shearing effects, however, can be neglected if the characteristic azimuthal wavelength of the instability is sufficiently large. This approach has been followed by Acheson [40], who derived a dispersion relation whose predictions have been compared with our numerical simulation results.

We have shown that this local linear analysis correctly predicts the unstable fluid regions in all the numerical simulations explored. When comparing the growth rates of the unstable azimuthal modes m, however, certain discrepancies occur in a few cases. The linear theory successfully predicts the most unstable azimuthal modes and their growth rates in runs at low Pm, whereas their values are overestimated in runs at $\mathrm{Pm} = 6$ and 8. We claim that shearing effects, associated with time-dependent unstable radial wave numbers, are likely more relevant in these latter cases and play a role to explain the observed differences. Enhanced dissipative effects acting on the small-scale sheared modes could provide an additional stabilising mechanism leading to the small growth rates observed.

It is important to stress that the local linear analysis employed, with all its simplifying assumptions, can only crudely describe the properties of the global modes excited in our numerical simulations. Differences of a small numerical factor in the predicted most unstable mode and growth rate, such as those observed here, are indeed not uncommon for this type of analysis (see, e.g., [35,59]) and should not be overinterpreted.

The study of the stability of dominantly toroidal magnetic field configurations, such as those considered in this work, is certainly relevant for stellar and planetary interiors. Due to the extremely high magnetic conductivity of the plasma in stellar interiors, for example, the magnetic Reynolds number Rm is so large that even a weak differential rotation can produce strong toroidal fields. Whereas our numerical simulations fall within this large-Rm regime, the values of $\mathrm{Pm} > 1$ we explored are far too large for stellar internal regions where viscosity is the smallest diffusivity (in the radiative core of the Sun, for example, $\mathrm{Pm} \approx 10^{-3}$). Small values of Pm are also typical of liquid metals employed in laboratory experiments of magnetic spherical Couette flow [18,20,31]. According to our numerical simulations, the critical value of Lo_φ for the MRI onset increases when Pm decreases. In the astrophysically relevant regime of $\mathrm{Pm} \ll 1$, it is therefore possible that the type of MRI studied here cannot develop since the large azimuthal field strengths likely required would modify the basic axisymmetric flow beforehand.

In this work we focused on the analysis of the linear properties of the instability, while exploring its nonlinear evolution and the saturation mechanism are deferred to future study. Preliminary results in this context show that the instability can modify the background shear by broadening and flattening the internal rotation contrast, as likewise described in similar setups by Petitdemange *et al.* [35,66]. As discussed in the Introduction, understanding the efficiency of MHD instabilities in redistributing the angular momentum is a question of primary astrophysical interest and could help shed light on puzzling helioseismic and asteroseismic observations such as the almost rigid rotation of the Sun's radiative core and the reduced internal rotation rates of subgiant and red giant stars.

Given the large values of Rm of the numerical simulations in the present study, we comment on the possibility of MRI-driven dynamo action. Self-sustained magnetic fields produced by MHD instabilities of hydrodynamically stable shear flows are generally thought to maintain turbulence in accretion disks, but may also develop in stably stratified stellar interiors [7]. Dynamo action relying on the MRI of toroidal magnetic fields in Keplerian shear flows was first observed in local shearing-box simulations [67] and later in more realistic setups such as rotating plane Couette flow [38]. More recently, Guseva *et al.* [39] reported numerical evidence of such a

dynamo in a global Taylor-Couette geometry with an imposed azimuthal field. Studies in a spherical shell and with more general field configurations such as those considered here are still lacking, but they certainly deserve attention since they are more directly relevant to stellar and planetary interiors.

ACKNOWLEDGMENTS

The authors acknowledge financial support from the Agence Nationale de la Recherche through the project IMAGINE (Grant No. ANR-13-BS05-0006). Computing time was provided by the HPC resources of CALMIP under Allocations No. 2016A-P1118, No. 2016B-P1118, No. 2017A-P1118, and No. 2017B-P1118. The authors wish to thank the two anonymous reviewers for their valuable comments and gratefully acknowledge L. Petitdemange and F. Stefani for helpful discussions.

APPENDIX: LOCAL DISPERSION RELATION

We examine herein the local dispersion relation in Acheson [40] that we used to interpret the instability found in our numerical simulations. First, we detail the assumptions employed in the local linear stability analysis. Then we derive a simplified version of the dispersion relation relevant for our study where no buoyancy is present. Finally, we comment on the validity of the linear analysis assumptions for our numerical simulations.

Acheson [40] studied the linear stability of an electrically conducting fluid rotating with angular velocity $\Omega(s,z)$ about the z axis of a cylindrical coordinate system (s,φ,z) in the presence of an axisymmetric azimuthal magnetic field $B_\varphi(s,z)$. The fluid is assumed incompressible under the Boussinesq approximation and stably stratified, with uniform kinematic viscosity ν, magnetic diffusivity η, and thermal diffusivity κ. The stability analysis is purely local in the sense that it is valid only in a small neighbourhood of a point (s,z). Two further assumptions are adopted. The first is the short-wavelength approximation

$$\lambda_{\rm m} \ll r, H_B, H_\Omega. \tag{A1}$$

Here $\lambda_{\rm m}=(\lambda_s^2+\lambda_z^2)^{1/2}$ denotes the meridional perturbation wavelength, $r=(s^2+z^2)^{1/2}$ the spherical radius, and $H_B=|B_\varphi/\nabla B_\varphi|$ ($H_\Omega=|\Omega/\nabla\Omega|$) the scale height of the azimuthal field (angular velocity). The second assumption concerns the azimuthal wavelength of the perturbation λ_φ, which satisfies

$$\lambda_{\rm m} \ll \lambda_\varphi. \tag{A2}$$

The MHD equations governing the system are linearized around the background axisymmetric state and, by considering small-amplitude harmonic perturbations in space and time of the form

$$\exp[i(k_s s + k_z z + m\varphi - \sigma t)], \tag{A3}$$

a dispersion relation is derived [Eq. (3.20) in 40]. Here $k_s=2\pi/\lambda_s$ ($k_z=2\pi/\lambda_z$) is the radial (vertical) wave number of the perturbation and m its azimuthal order which is an $O(1)$ integer. When the imaginary part of σ is positive, the applied perturbation is unstable and grows exponentially at a rate $\gamma=\mathrm{Im}(\sigma)$.

If the fluid has no buoyancy, as in our setup, the dispersion relation reduces to

$$u_{\rm A}^2\left[\frac{2\Omega m}{s}+(\omega+i\nu k^2)\frac{2}{s}\right]\left[\frac{m}{\omega+i\eta k^2}\frac{\partial\Omega}{\partial h}+\frac{\partial Q}{\partial h}-\frac{2}{s}\right]+\left[\frac{k^2}{k_z^2}\left(\omega+i\nu k^2-\frac{m^2u_{\rm A}^2}{s^2}\frac{1}{\omega+i\eta k^2}\right)\right]$$
$$\times\left[(\omega+i\nu k^2)(\omega+i\eta k^2)-\frac{m^2u_{\rm A}^2}{s^2}\right]-\left[\frac{\partial(\Omega s^2)}{\partial h}+\frac{m\,u_{\rm A}^2}{\omega+i\eta k^2}\frac{\partial Q}{\partial h}\right]\left[\frac{2\Omega}{s}(\omega+i\eta k^2)+\frac{2mu_{\rm A}^2}{s^3}\right]=0, \tag{A4}$$

where $\omega=\sigma-m\Omega$ is the Doppler-shifted frequency, $u_{\rm A}=B_\varphi/\sqrt{\mu\rho}$ is the Alfvén velocity, $k^2=k_s^2+k_z^2$, $Q=\ln(sB_\varphi)$, and finally

$$\frac{\partial}{\partial h}=\frac{\partial}{\partial s}-\frac{k_s}{k_z}\frac{\partial}{\partial z} \tag{A5}$$

defines the meridional derivative. When written as a polynomial equation in the dimensionless frequency $\tilde\omega=\omega/\Omega$, Eq. (A4) reads

$$\sum_{i=0}^{4} a_i\tilde\omega^i=0, \tag{A6}$$

where

$$a_4=1+\beta^2, \tag{A6a}$$

$$a_3=i\big[2(1+\beta^2)\big(R_e^{-1}+R_m^{-1}\big)\big], \tag{A6b}$$

$$a_2=-2(q+2)+2L_o^2[b-1-(1+\beta^2)m^2]-(1+\beta^2)\big(R_e^{-2}+R_m^{-2}-4R_e^{-1}R_m^{-1}\big), \tag{A6c}$$

$$a_1=-8mL_o^2+i\big\{2L_o^2[b-1-(1+\beta^2)m^2]\times\big[R_e^{-1}+R_m^{-1}\big]-4(2+q)R_m^{-1}-2(1+\beta^2)\big(R_e^{-2}R_m^{-1}+R_e^{-1}R_m^{-2}\big)\big\}, \tag{A6d}$$

$$a_0=m^2L_o^2\big\{2q-L_o^2[2(b+1)-(1+\beta^2)m^2]\big\}-2L_o^2[b-1-(1+\beta^2)m^2]R_e^{-1}R_m^{-1}+(1+\beta^2)R_e^{-2}R_m^{-2}+2(2+q)R_m^{-2}+i\big\{2mL_o^2\big[qR_e^{-1}-(4+q)R_m^{-1}\big]\big\}. \tag{A6e}$$

The dispersion relation coefficients a_i depend on six dimensionless parameters: the poloidal wave number ratio

$$\beta=\frac{k_s}{k_z}, \tag{A7a}$$

TABLE III. Measures used to test the validity of the local linear analysis assumptions in the numerical simulation runs explored. Columns 2 and 3 compare the characteristic meridional instability length scale $\overline{\lambda}_\mathrm{m}$ with estimates of the scale heights of the axisymmetric azimuthal field and the angular velocity, respectively (see the main text for further details). The last column lists the ratio of the characteristic meridional instability length scale to the azimuthal one.

Run	$\overline{\lambda}_\mathrm{m}\langle\lvert H_B\rvert^{-1}\rangle$	$\overline{\lambda}_\mathrm{m}\langle\lvert H_\Omega\rvert^{-1}\rangle$	$\overline{\lambda}_\mathrm{m}/\overline{\lambda}_\varphi$
Pm2	0.59	1.1×10^{-2}	0.38
Pm3	0.50	1.0×10^{-2}	0.34
Pm6a	0.33	6.6×10^{-3}	0.35
Pm6b	0.33	6.4×10^{-3}	0.27
Pm6c	0.36	6.8×10^{-3}	0.29
Pm8b	0.33	5.5×10^{-3}	0.30

the shear parameter

$$q=\frac{\partial\ln\Omega}{\partial\ln s}-\beta\frac{s}{z}\frac{\partial\ln\Omega}{\partial\ln z}, \tag{A7b}$$

a parameter associated with the magnetic field derivatives

$$b=\frac{1}{2}\left(\frac{\partial\ln B_\varphi^2}{\partial\ln s}-\beta\frac{s}{z}\frac{\partial\ln B_\varphi^2}{\partial\ln z}\right), \tag{A7c}$$

the local azimuthal Lorentz number

$$L_o=\frac{\omega_\mathrm{A}}{\Omega}, \tag{A7d}$$

where $\omega_\mathrm{A}=B_\varphi/\sqrt{\mu\rho}\,s$ is the Alfvén frequency, and finally the hydrodynamical and magnetic Reynolds numbers

$$R_e=\frac{\Omega}{\nu k^2}\quad\text{and} \tag{A7e}$$

$$R_m=\frac{\Omega}{\eta k^2}. \tag{A7f}$$

We now discuss how well the linear analysis assumptions on the perturbation wavelengths are satisfied in our numerical simulations. First, we examine the short-wavelength approximation (A1). To this end, we compare the characteristic meridional instability length scale with the scale heights of the perturbed axisymmetric solution in the numerical simulation runs discussed in Secs. V and VI. As reported in the second column of Table III, the product $\overline{\lambda}_\mathrm{m}\langle\lvert H_B\rvert^{-1}\rangle$ is smaller than 0.6 in all runs explored. Here

$$\overline{\lambda}_\mathrm{m}=\left(\overline{\lambda}_s^{-2}+\overline{\lambda}_z^{-2}\right)^{1/2}$$

and

$$\langle\lvert H_B\rvert^{-1}\rangle=[(\langle\lvert H_{B,s}\rvert^{-1}\rangle)^2+(\langle\lvert H_{B,z}\rvert^{-1}\rangle)^2]^{1/2}$$

are estimates of the meridional instability length scale and of the inverse absolute field scale height, respectively ($H_{B,s}$ and $H_{B,z}$ are the field scale heights in the s and z directions, respectively). The overbar and the angular brackets denote, respectively, the mean and the meridional average described in Sec. VI B. Local values of $\overline{\lambda}_\mathrm{m}\lvert H_B\rvert^{-1}$ in the unstable fluid regions are of about 2 at most. This typically occurs at locations close to the inner and outer shell boundaries where the azimuthal field gradients are large due to the electrically insulating boundary conditions. However, the instability mode amplitude is small or negligible in these regions (see Fig. 9, right panels).

Concerning the angular velocity scale heights, values of $\overline{\lambda}_\mathrm{m}\lvert H_\Omega\rvert^{-1}$ never exceed 0.02 in the unstable regions for all the runs analyzed. The estimates $\overline{\lambda}_\mathrm{m}\langle\lvert H_\Omega\rvert^{-1}\rangle$ are also small, typically below 0.01 (see Table III, column 3). All the above observations show that the short-wavelength assumption (A1) is not violated in the numerical simulations considered in this study.

The second assumption (A2) requires an azimuthal wavelength of the instability much larger than the meridional one. The ratio $\overline{\lambda}_\mathrm{m}/\overline{\lambda}_\varphi$ ranges from about 0.3 to roughly 0.4 in the runs explored (Table III, column 4), thus marginally satisfying also this second assumption.

[1] X. Song and P. G. Richards, Nature (London) **382**, 221 (1996).
[2] J. E. Vidale, D. A. Dodge, and P. S. Earle, Nature (London) **405**, 445 (2000).
[3] S. Deheuvels, R. A. García, W. J. Chaplin, S. Basu, H. M. Antia, T. Appourchaux, O. Benomar, G. R. Davies, Y. Elsworth, L. Gizon *et al.*, Astrophys. J. **756**, 19 (2012).
[4] B. Mosser, M. J. Goupil, K. Belkacem, J. P. Marques, P. G. Beck, S. Bloemen, J. De Ridder, C. Barban, S. Deheuvels, Y. Elsworth, S. Hekker, T. Kallinger, R. M. Ouazzani, M. Pinsonneault, R. Samadi, D. Stello, R. A. García, T. C. Klaus, J. Li, S. Mathur, and R. L. Morris, Astron. Astrophys. **548**, A10 (2012).
[5] S. Deheuvels, G. Doğan, M. J. Goupil, T. Appourchaux, O. Benomar, H. Bruntt, T. L. Campante, L. Casagrande, T. Ceillier, G. R. Davies *et al.*, Astron. Astrophys. **564**, A27 (2014).
[6] J. P. Marques, M. J. Goupil, Y. Lebreton, S. Talon, A. Palacios, K. Belkacem, R. M. Ouazzani, B. Mosser, A. Moya, P. Morel, B. Pichon, S. Mathis, J. P. Zahn, S. Turck-Chièze, and P. A. P. Nghiem, Astron. Astrophys. **549**, A74 (2013).
[7] H. C. Spruit, Astron. Astrophys. **381**, 923 (2002).
[8] G. Rüdiger, M. Gellert, F. Spada, and I. Tereshin, Astron. Astrophys. **573**, A80 (2015).
[9] F. Spada, M. Gellert, R. Arlt, and S. Deheuvels, Astron. Astrophys. **589**, A23 (2016).
[10] I. Proudman, J. Fluid Mech. **1**, 505 (1956).
[11] K. Stewartson, J. Fluid Mech. **26**, 131 (1966).
[12] R. Hollerbach, Proc. R. Soc. A **444**, 333 (1994).
[13] E. Dormy, P. Cardin, and D. Jault, Earth Planet. Sci. Lett. **160**, 15 (1998).
[14] R. Hollerbach, in *Physics of Rotating Fluids*, edited by C. Egbers and G. Pfister (Springer, Berlin, 2000), pp. 295–316.
[15] R. Hollerbach, in *Dynamo and Dynamics: A Mathematical Challenge*, edited by P. Chossat, D. Ambruster, and I. Oprea (Springer Netherlands, Dordrecht, 2001), pp. 189–197.

[16] R. Hollerbach and S. Skinner, Proc. R. Soc. A **457**, 785 (2001).
[17] X. Wei and R. Hollerbach, Phys. Rev. E **78**, 026309 (2008).
[18] H. C. Nataf, T. Alboussière, D. Brito, P. Cardin, N. Gagnière, D. Jault, J. P. Masson, and D. Schmitt, Geophys. Astrophys. Fluid Dyn. **100**, 281 (2006).
[19] R. Hollerbach, E. Canet, and A. Fournier, Eur. J. Mech. B **26**, 729 (2007).
[20] C. Kasprzyk, E. Kaplan, M. Seilmayer, and F. Stefani, Magnetohydrodynamics **53**, 393 (2017).
[21] E. P. Velikhov, Sov. Phys. JETP **36**, 995 (1959).
[22] S. Chandrasekhar, Proc. Natl. Acad. Sci. USA **46**, 253 (1960).
[23] S. A. Balbus and J. F. Hawley, Astrophys. J. **376**, 214 (1991).
[24] S. A. Balbus and J. F. Hawley, Astrophys. J. **400**, 610 (1992).
[25] G. I. Ogilvie and J. E. Pringle, Mon. Not. R. Astron. Soc. **279**, 152 (1996).
[26] G. Rüdiger, R. Hollerbach, M. Schultz, and D. A. Shalybkov, Astron. Nachr. **326**, 409 (2005).
[27] G. Rüdiger, R. Hollerbach, M. Gellert, and M. Schultz, Astron. Nachr. **328**, 1158 (2007).
[28] R. Hollerbach, V. Teeluck, and G. Rüdiger, Phys. Rev. Lett. **104**, 044502 (2010).
[29] G. Rüdiger, M. Gellert, R. Hollerbach, M. Schultz, and F. Stefani, Phys. Rep. **741**, 1 (2018).
[30] M. Seilmayer, V. Galindo, G. Gerbeth, T. Gundrum, F. Stefani, M. Gellert, G. Rüdiger, M. Schultz, and R. Hollerbach, Phys. Rev. Lett. **113**, 024505 (2014).
[31] D. R. Sisan, N. Mujica, W. A. Tillotson, Y.-M. Huang, W. Dorland, A. B. Hassam, T. M. Antonsen, and D. P. Lathrop, Phys. Rev. Lett. **93**, 114502 (2004).
[32] R. Hollerbach and G. Rüdiger, Phys. Rev. Lett. **95**, 124501 (2005).
[33] C. Gissinger, H. Ji, and J. Goodman, Phys. Rev. E **84**, 026308 (2011).
[34] L. Petitdemange, E. Dormy, and S. A. Balbus, Geophys. Res. Lett. **35**, L15305 (2008).
[35] L. Petitdemange, E. Dormy, and S. Balbus, Phys. Earth Planet. Inter. **223**, 21 (2013).
[36] C. Guervilly and P. Cardin, Geophys. Astrophys. Fluid Dyn. **104**, 221 (2010).
[37] F. Marcotte and C. Gissinger, Phys. Rev. Fluids **1**, 063602 (2016).
[38] F. Rincon, G. I. Ogilvie, and M. R. E. Proctor, Phys. Rev. Lett. **98**, 254502 (2007).
[39] A. Guseva, R. Hollerbach, A. P. Willis, and M. Avila, Phys. Rev. Lett. **119**, 164501 (2017).
[40] D. J. Acheson, Philos. Trans. R. Soc. London Ser. A **289**, 459 (1978).
[41] U. R. Christensen and J. Aubert, Geophys. J. Int. **166**, 97 (2006).
[42] J. Wicht, Phys. Earth Planet. Inter. **132**, 281 (2002).
[43] N. Schaeffer, Geochem. Geophys. Geosyst. **14**, 751 (2013).
[44] https://magic-sph.github.io.
[45] U. R. Christensen and J. Wicht, in *Treatise on Geophysics*, 2nd ed., edited by G. Schubert (Elsevier, Oxford, 2015), pp. 245–277.
[46] R. Hollerbach, J. Fluid Mech. **492**, 289 (2003).
[47] J. Wicht, J. Fluid Mech. **738**, 184 (2014).
[48] N. Schaeffer and P. Cardin, Phys. Fluids **17**, 104111 (2005).
[49] R. J. Tayler, Mon. Not. R. Astron. Soc. **161**, 365 (1973).
[50] M. Goossens and R. J. Tayler, Mon. Not. R. Astron. Soc. **193**, 833 (1980).
[51] E. Pitts and R. J. Tayler, Mon. Not. R. Astron. Soc. **216**, 139 (1985).
[52] E. Knobloch, in *Lectures on Solar and Planetary Dynamos*, edited by M. R. E. Proctor and A. D. Gilbert (Cambridge University Press, Cambridge, 1994), pp. 331–372.
[53] O. N. Kirillov, F. Stefani, and Y. Fukumoto, Astrophys. J. **756**, 83 (2012).
[54] G. Rüdiger, M. Gellert, M. Schultz, R. Hollerbach, and F. Stefani, Mon. Not. R. Astron. Soc. **438**, 271 (2014).
[55] F. Stefani, T. Gundrum, G. Gerbeth, G. Rüdiger, M. Schultz, J. Szklarski, and R. Hollerbach, Phys. Rev. Lett. **97**, 184502 (2006).
[56] G. Rüdiger, R. Hollerbach, F. Stefani, T. Gundrum, G. Gerbeth, and R. Rosner, Astrophys. J. Lett. **649**, L145 (2006).
[57] F. Stefani, T. Gundrum, G. Gerbeth, G. Rüdiger, J. Szklarski, and R. Hollerbach, New J. Phys. **9**, 295 (2007).
[58] G. Rüdiger, M. Schultz, M. Gellert, and F. Stefani, J. Plasma Phys. **84**, 735840101 (2018).
[59] L. Jouve, T. Gastine, and F. Lignières, Astron. Astrophys. **575**, A106 (2015).
[60] S. A. Balbus and J. F. Hawley, Rev. Mod. Phys. **70**, 1 (1998).
[61] K. Julien and E. Knobloch, Philos. Trans. R. Soc. A **368**, 1607 (2010).
[62] Y. Masada, T. Sano, and H. Takabe, Astrophys. J. **641**, 447 (2006).
[63] J. Squire and A. Bhattacharjee, Astrophys. J. **797**, 67 (2014).
[64] R. Hollerbach, Proc. R. Soc. A **465**, 2003 (2009).
[65] L. L. Kitchatinov and G. Rüdiger, Astron. Astrophys. **513**, L1 (2010).
[66] L. Petitdemange, Geophys. Astrophys. Fluid Dyn. **104**, 287 (2010).
[67] J. F. Hawley, C. F. Gammie, and S. A. Balbus, Astrophys. J. **440**, 742 (1995).